Millilensing statistics for BH clusters and Gaussian subhaloes

Tutor:	Evencio Mediavilla Gradolph
Author:	Guillermo Rodríguez Vega

July 4, 2024

Contents

Abstract

The aim of this TFM is to probe candidates to Dark Matter through their effect on the probability density function of the magnification induced by gravitational lensing, $PDF(\mu)$. This is done by simulating the millilensing effect using the inverse ray tracing algorithm in both Python3 and FORTRAN95. Furthermore, we have implemented the nearest neighbours algorithm in the codes and performed a comparison of the computational efficiency between Python3 and FORTRAN95 scripts. To cross-check our numerical models we compare with the theoretical predictions for the sparse case. Our first candidates to dark matter are primordial black holes, which become an interesting possibility after LIGO-VIRGO observations. In this TFM we are considering them grouped in clusters of variable compactness, instead of following a random uniform distribution. Furthermore, we study whether at large scales a compact cluster behaves as a pseudo-particle being indistinguishable from a single black hole with the same mass of the cluster. Our second candidates under study are DM subhaloes. The existence of these subhaloes is predicted by CDM models of structure formation. We analyze whether the gravitational lensing magnification induced by DM Gaussian subhaloes with different compactness is consistent with real observations. A Bayesian analysis based on compactness and magnification shows that, according to observations, clustering

makes less probable the existence of PBH's and that a large compactness of the subhaloes should result in millilensing magnification larger than observed.

Resumen

El efecto lente gravitacional está predicho desde la formulación de la relatividad general, y de hecho uno de los test clásicos de esta teoría se realizó midiendo en 1919 la deflexión de la luz producida por el Sol. Desde entonces se han detectado distintos fenómenos relacionados con el efecto lente gravitatoria en el universo. Los más notables son los clasificados como eventos de lente fuertes producidos por un objeto (la lente) que divide la luz de una fuente (generalmente un quasar) en múltiples imágenes. Por otro lado, cuando la masa de la lente es relativamente pequeña y las imágenes no se pueden separar con los telescopios actuales, el fenómeno se conoce como micro/mililensing. Este efecto es una de las principales herramientas para probar la naturaleza de la Materia Oscura. El objetivo de este TFM es valorar dos posibles candidatos a Materia Oscura. En primer lugar los PBH's, Primordial Black Holes (Agujeros negros primordiales), que a diferencia de otros estudios [1], vamos a considerar organizados en cúmulos. La existencia de PBH's está apoyada en observaciones de LIGO-VIRGO. Desde la detección de la primera onda gravitacional en 2016, se han sumado otras observaciones que han llevado a la conclusión de que la presencia de agujeros negros de masa intermedia $3M_\odot \leq M \leq 60M_\odot$ es significativa [1]. Por otro lado, las teorías sobre el origen de los PBH's predicen que se forman en cúmulos [2]. Un segundo candidato a deflector son los subhalos de materia oscura, predichos en modelos de formación de estructuras basados en CDM. Estudiaremos estos dos candidatos a lente gravitacional considerando diferentes grados de compacidad, a través su efecto sobre la función de densidad de probabilidad de magnificación inducida por el efecto lente gravitacional $PDF(\mu)$. Con este objetivo construiremos mapas de magnificación. Dado que la ecuación de la lente no tiene por lo general una solución analítica, los mapas se calcularán usando métodos numéricos, en particular el algoritmo de trazado de rayos inverso (IRS), con programas escritos en Python3 y en FORTRAN95. Al código de IRS le implementaremos un algoritmo de próximos para obtener mapas menos ruidosos. Debido a la versatilidad y flexibilidad de este lenguaje, comenzamos a hacer las simulaciones del TFM con Python3, sin embargo el tiempo de ejecución es demasiado elevado, y decidimos cambiar el código a FORTRAN95. Un análisis comparativo en el que hemos investigado la dependencia del tiempo de ejecución con el número de rayos, nos ha llevado a la conclusión de que el tiempo de ejecución se reduce en un factor 17 en promedio, cambiando el código de Python3 a FORTRAN95. Sin embargo, para los cálculos masivos que hemos necesitado hacer, la eficiencia del IRS incluso con FORTRAN95 no es suficiente y hemos tenido que hacer uso del algoritmo inverse polygon mapping (IPM) descrito en [3]. Este algoritmo se ejecuta en la página web: https://gloton.ugr.es/microlensing/, y por defecto creará una distribución uniforme de lentes. En el caso de que queramos estudiar una distribución de lentes agrupadas en cúmulos, tendremos que suministrar nosotros la distribución espacial de los agujeros negros. La eficiencia computacional es muy importante en este TFM, dado que necesitamos hacer un gran número de realizaciones, debido a que las PDF's son muy sensibles a la varianza muestral. Se han calculado miles de simulaciones (mapas de magnificación) de las cuales hemos usado 553 en la versión final del TFM. Para asegurarnos de que nuestros métodos son correctos verificaremos nuestras simulaciones con la solución teórica disponible para el caso de lentes dispersas. Una distribución de micro/mililentes se considera dispersa cuando en una región de varios radios de Einstein alrededor de cada microlente la desviación de los rayos de luz depende marginalmente del resto de las microlentes. Los resultados de este análisis muestran un buen acuerdo entre la expresión teórica de la PDF y la PDF obtenida de las simulaciones. No obstante, encontramos un abultamiento en la PDF de las simulaciones producidas por las caústicas que no está predicha en la expresión teórica y una desviación respecto al comportamiento asintótico para altas magnificaciones debida a la limitada resolución del mapa (el tamaño del pixel). Una vez comprobado que nuestras simulaciones reproducen los resultados teóricos correctamente estudiamos el efecto de los cúmulos de PBH's a grandes y pequeñas escalas en los mapas de magnificación y en las PDF's, llegando a la conclusión de que cuando un cúmulo es suficientemente compacto, este es indistinguible de una lente puntual, produciendo una única escala de grandes caústicas en el mapa de magnificación. Cuando el cúmulo no es tan compacto puede percibirse una segunda estructura de caústicas a escala más pequeña producida por los PBH individuales. Es decir, hemos comprobado que los cúmulos a una escala suficientemente grande se comportan como una pseudo-partícula. Una vez analizado el efecto de los cúmulos a distintas escalas, antes de continuar con los objetivos del TFM hay que tener en cuenta que dado que cada realización depende altamente de la distribución de lentes y cúmulos, estos tendrán un significativo ruido poissoniano, por lo que será necesario promediar 50 realizaciones de cada caso. El siguiente paso es estudiar como varían las PDF's de los cúmulos de PBH's con la compacidad, considerando un tamaño constante y variando el numero de BH's por cúmulo. Un análisis Bayesiano basado

en valores típicos observados de las anomalías de flujo en sistemas múltiples de quasares, indica que la probabilidad de reproducir las observaciones disminuye con la compacidad. Es decir, el agrupamiento en cúmulos hace menos probable la existencia de PBH's. En la segunda parte del TFM estudiamos distribuciones de subhalos, considerando que su perfil radial de masa es Gaussiano, para simplificar el analisis. Para hacer un test de nuestras simulaciones, también en este caso, comparamos la PDF de la lente Gaussiana a muy alta compacidad con la PDF de la lente puntual, la cual debería ser su caso límite. A continuación, analizamos las PDF's de los subhalos Gaussianos a distinta compacidad, determinando que también en este caso la probabilidad de las altas magnificaciones aumenta con la compacidad. Finalmente, el análisis Bayesiano basado en la compacidad de los subhalos Gaussianos y las anomalías de flujo observadas, muestra que, solo subhalos de baja compacidad pueden explicar las observaciones.

1 Introduction

Light deflection by matter had great importance in the history of modern physics, in fact one of the classical tests of general relativity was made by Eddington's team, when they measured the apparent displacement of the stars induced by the Sun's gravity during the solar eclipse of 1919, in agreement with the predictions of Einstein's theory [4]. Nowadays gravitational lensing is a widely used tool in many kinds of researches, like the discovery of Eärendel, the more distant star ever found, or the study of dark matter and cosmology.

1.1 General relativity and lensing

Certainly, gravitational lensing is a consequence of general relativity, which established that gravity was a curvature in space-time and not a force. The key idea is that mass modifies the surrounding space-time making light to bend as it pass through. The fundamental equations describing this space-time curvature are known as the Einstein field equations:

$$G_{\mu\nu} + \Lambda g_{\mu\nu} = \frac{8\pi G}{c^4} T_{\mu\nu}. \tag{1}$$

Applying these field equations considering the general symmetries of a space-time metric surrounding a static point mass M would lead to Schwarzschild metric:

$$ds^2 = \left(1 - \frac{2GM}{rc^2}\right) c^2 dt^2 - \left(1 - \frac{2GM}{rc^2}\right)^{-1} dr^2 - r^2 d\theta^2 - r^2 \sin^2\theta d\phi^2 \tag{2}$$

From the metric in the weak field approximation the expression of the angle of deflection of the light rays, $\hat{\alpha}$, can be derived. This is the only equation from general relativity that we need for our work:

$$\hat{\alpha} = \frac{4GM}{rc^2} [5] \tag{3}$$

1.2 Gravitational lensing and types of lensing

Even though general relativity was demonstrated by gravitational lensing in 1919, it was unclear at this epoch whether the study of light bending would have a future in its own right. Indeed, Einstein considering star by star lensing dismissed the possibility that phenomena such as multiple images could actually be observed. It was not until 1979 that with the discovery of the quasar Q0957+561 lensed by a galaxy, it was confirmed that gravitational lensing is a common phenomenon in the universe [4].

(a) Hubble Space Telescope image of the strong lens system Q0957+561. The two bright spots of the centre are in fact the same quasar lensed by the galaxy in between.

(b) Hubble Space Telescope image of the galaxy cluster Abell 370. The long structure to the lower left of the center was the first lensed arc to be discovered. This kind of events are tricky since separate lensed images can merge together, creating structures that are visually striking but may be hard to identify.

Figure 1: Hubble Space Telescope images of strong lensing events [4].

Gravitational lensed systems like Q0957+561 are classified as strong lensing events, as they consist on an intervening object (the lens) which splits the light from a more distant source into multiple images [4]. In Q0957+561 the faraway object is a quasar lensed by a galaxy cluster. Moreover these strong lensing events are not common to observe as it is needed that the quasar, the cluster and the Earth are aligned.

On the other hand, when the mass of the lens is relatively small and the images cannot be separated, the magnification phenomenon of the background source produced by the foreground lens is known as microlensing, which cannot be identified in a single epoch observation because we do not know the intrinsic brightness of the object. However, the change in magnification resulting from the relative motion of the observer, lens, and source, which occurs on timescales of months or years can be measured. Einstein dismissed such lensing phenomenon in the context of star by star lensing, but nowadays it is measurable with the advances of technology and indeed the study of microlensing helped to demonstrate that massive astrophysical compact halo objects (MACHOs), including brown dwarfs and a variety of stellar remnants exist in quantities too small to account for the DM [4].

Moreover, if the spatial scale for these perturbations is typically of a few to tens of milliarcseconds, the phenomenon is referred to as millilensing, and at difference from microlensing which is typically produced by stars, these millilensing events could be produced by galactic substructures of DM or by large mass BH's [4].

1.3   Dark Matter and Galactic substructures

The deviation of light induced by a massive object is one of the clues that modern physics has for the existence of DM. Since the discovery of the "Missing Mass" problem, several candidates to DM have been considered. They can be grouped into two types; elementary particles known as WIMP (Weakly interacting massive particle) and compact objects; like MACHO (Massive Compact Halo Objects) or BH's.

DM as a elementary particle is the main hypothesis and is included in the nowadays standard model of cosmology CDM (Cold Dark Matter), which considers DM to be non-baryonic matter produced in the early stages of the Big Bang, hence not related to the nucleosynthesis [5]. These particles would have slow velocities, contrary to other models like HDM (Hot Dark Matter) which considers DM to be relativistic particles [6]. Nevertheless, for the time being particle physics is unable to find a reliable

candidate particle, following the CDM model, to explain DM [7].

The statistical amount of MACHOs in our galaxy can not explain its dark mass, so this is not a current line of research and lower masses than $1M_\odot$ are excluded by galactic microlensing experiments, [7] so we are running out of candidates. However, compatible with cosmological nucleosynthesis calculations, at least part of this mass must be in the form of non-baryonic particles or perhaps primordial BH's which formed before nucleosynthesis and therefore did not participate in it [5]. Moreover, LIGO (and VIRGO) experiments show that DM could consist of primordial BH's with masses $1M_\odot < M < 1000M_\odot$ [7].

Simulations of structure formation, based on CDM model show that a halo of mass M contains numerous halos of much lower mass, the subhaloes [6]. This can be expected because clusters of galaxies contain substructures, visible in the form of the cluster galaxies. Some of these substructures are recognized in our Milky Way, known as satellite galaxies like the Magellanic Clouds. However, fewer than 40 members of the Local Group are known whereas the numerical simulations predict hundreds of satellite galaxies for the Galaxy. This deficit is known as the "Missing Satellites Problem" [6]. This could suggest that the visible satellites are a subset of a large population of subhaloes, and the rest remained like bound clumps of DM that orbit within the galaxy's overall DM halo [4].

1.4   Primordial Black holes formation

There are several models of PBH's formation. They can be formed at the early dust-like stages, or at stages of a dominance of dissipative superheavy metastable particles owing to a rapid evolution of star-like objects, or even PBH's can be formed from the baryon charge fluctuations. Another formation schemes are considered in inflationary models. [2]

The standard cosmological model CDM presents several unsolved issues. That is why inflation theory arises to solve some of the main problems of CDM model; such as the flatness problem, the cosmological horizon problem or the monopole problem. [5]. As inflation is subdued to quantum physics then it would present quantum fluctuations, which would lead to the formation of closed domain walls. After the inflation is finished, the walls could collapse into BH's in the final state. The so-called primordial black holes (PBH) [2].

Inflationary models establish that these PBH's could have formed grouped in clusters. This fact can be supported by the BH's mergers detected by LIGO-VIRGO. These clusters would consist in a PBH in company of BH's of smaller mass, which eventually would merge, forming PBH's around the original one (the parent PBH), giving rise to a fractal structure [2]. The study of the gravitational lensing magnification induced by these BH's clusters could give us a clue about whether they are a viable solution for the DM problem.

2   Motivation and Objectives

As commented in the Introduction, DM is one of the biggest problems in modern physics. In the actual paradigm it is widely accepted its existence. In particular, its effect is very notable in gravitational lensing. Although there are many others phenomena like the measurement of the rotation profile of galaxies or the bullet cluster that otherwise would not have a satisfactory explanation without DM.

DM is an important ingredient in the cosmological model, CDM, as well as Dark Energy or the Inflationary field. This is, among other reasons, because DM accelerates structure formation such as galaxies. It is located forming a halo surrounding their galaxies (wider than the galactic halo) and in a cosmological large scale forming cosmic webs. The candidate that makes up DM must fulfill these conditions. The lack of evidence of candidates such as compact objects like MACHO or BH's from a stellar origin, or elementary particles leads to consider other alternatives like PBH's.

Observations from LIGO-VIRGO give support to consider PBH's as a non-negligible alternative to DM. Since the first detection of a gravitational wave in 2016, other observations have been added that led to the idea that the presence of BH's of intermediate mass $3M_\odot \leq M \leq 60M_\odot$ is significant.

As the masses detected by LIGO were significantly larger than originally expected for BH's of stellar origin, this detection renewed the interest in PBH's as DM constituents [1].

An interesting way, in the context of gravitational lensing to detect the PBH's is through the micro/millilensing effect. Until now, the published studies [1] indicate that if the DM were formed by PBH's, the expected flux anomalies caused by micro/millilensing should be larger than the ones observed. However, these studies focus on a random uniform distribution of non clustered BH.

Consequently, the first objective of this TFM is to study the effect of the clustering of BH's, analyzing how the compactness of these clusters induces anomalies in the flux ratios of the images of lensed quasars via the millilensing effect. This will be done modifying two variables; the number of BH's per cluster and the size of these clusters. In order to do this, we use in the first place, our own simulation scripts written in Fortran95 and Python3. Some of the simulations will require a more sophisticated online software to use the Inverse Polygonal Mapping algorithm described in [3].

Using PDF's of the magnifications induced by millilensing conditioned to different compactness of the clusters and observed magnifications, we will perform a Bayesian analysis to infer the most probable cluster's compactness.

The second objective of this TFM is to study the compactness of subhaloes and its effect on the millilensing. As commented in the Introduction, CDM model predicts an amount of substructures in the DM haloes in the form of subhaloes or satellites that is much higher than the number of luminous satellites observed around the Milky Way [8] (Missing Satellites Problem). So, in the second part of the TFM we are going to simulate Gaussian subhaloes of different compactness, calculating the expected PDF's of the magnifications and comparing the results with the observations.

3   Methods

To introduce gravitational lensing simulations it is convenient to very briefly review the basis of lensing theory. Starting with the geometry of light bending and continuing with how should this effect be simulated.

3.1   The Lens Equation and Image Magnification

Let S be a source, L a massive object that creates a gravitational field and O an observer. The light ray coming from S to O is bent by lens L creating an image I seen by observer O. The angle measured by the observer O between S and I is the deflection angle $\hat{\alpha}$, which expression is given by (Eq. 3) [4].
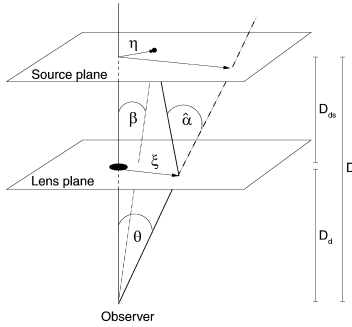

Figure 2: Gravitational lens system; being D_s the angular size distance between the observer and the source, D_d the distance from us of the lens, D_{ds} the distance between the source and the lens and $\hat{\alpha}$ is the deflection angle [6].

From similarities between triangles, the lens equation can be written as the following expression:

$$\vec{\eta}\frac{D_d}{D_s} = \vec{\xi} - \frac{D_{ds}D_d}{D_s}\hat{\alpha} \qquad (4)$$

6

The lens equation is multivaluated, since we can associate multiple images to the same source, so we need to invert and reduce it to its dimensionless equation. So considering that β is the true angular position of the source:

$$\beta = \frac{\eta}{D_s} \tag{5}$$

and being ξ the position of the light ray in the lens plane, its angular position θ will be given by:

$$\theta = \frac{\xi}{D_d} \tag{6}$$

and therefore from the general expression of the lens equation (Eq. 4), it can be defined the dimensionless deflection angle:

$$\vec{\alpha}(\theta) = \frac{D_{ds}}{D_s} \hat{\alpha}(D_d\theta), \tag{7}$$

and, finally, changing $\beta \to \vec{y}$ and $\theta \to \vec{x}$, then the reduced lens equation is given by the expression:

$$\vec{y} = \vec{x} - \vec{\alpha}(\vec{x}). \tag{8}$$

[6]
An image with position θ will be magnified by an amount $\mu(\theta)$ which satisfies:

$$|\mu| = \left| \frac{\theta d\theta}{\beta d\beta} \right|, \tag{9}$$

Since the reduced lens equation (Eq. 8) tells us how β depends on θ, it is easier to work with the inverse magnification:

$$\mu^{-1}(\theta) = \frac{\beta d\beta}{\theta d\theta} = \left(1 - \frac{\alpha}{\theta}\right)\left(1 - \frac{d\alpha}{d\theta}\right), \tag{10}$$

From (Eq. 10) it can be noted that the magnification diverges if either (or both) of the factors vanishes, i.e., if $\alpha = \theta$ or $d\alpha/d\theta = 1$. Values of θ that satisfy these relations are said to lie on critical curves. Under the lens equation, critical curves correspond to curves in the source plane called caustics [4].

Defining the Einstein radius as:

$$\xi_0 = \sqrt{\frac{D_{ds}}{D_d D_s} \frac{4GM}{c^2}} \, [4] \tag{11}$$

Using the Einstein radius as the unit allows us to work with masses on an arbitrary scale.

3.2 Inverse ray tracing

The lens equation (Eq. 8) in its general expression has one or several solutions. Analytically the equation can not be inverted except for some particular mass distribution of the lens but it can be numerically solved using the inverse ray tracing algorithm. The first thing to do, is to divide the source and image plane regions under study into pixels/cells: $F(i_1, i_2) \leftarrow F(\vec{y})$ and $I(j_1, j_2) \leftarrow I(\vec{x})$. Being $2x_l$ and $2y_l$ the size of the square regions at the lens and source planes. Hence, the size of the cells are $x_s = 2x_l/(n_x - 1)$ and $y_s = 2y_l/(n_y - 1)$. The algorithm starts reading the source as a matrix $F(i_1, i_2)$. Then at the image plane we can transform from pixel to coordinates:

$$x_1 = -x_l + (j_1 - 1)x_s + 1 \qquad\qquad x_2 = -x_l + (j_2 - 1)x_s + 1 \tag{12}$$

After that, it is applied the inverse transformation, which is always uni-valued, $\vec{x} \to \vec{y} = \vec{x}$. Next step, is to transform at the source plane from coordinate to pixel:

$$i_1 = \frac{y_1 + y_l}{y_s} \qquad\qquad i_2 = \frac{y_2 + y_l}{y_s} \tag{13}$$

Subsequently, it is checked if the image pixels are inside the considered region at the source plane to assign $I(j_1, j_2) = F(i_1, i_2)$, otherwise it is done $I(j_1, j_2) = C$ where C is sky's background constant (normally 0).

Simultaneously, it is built the magnification map of the lens by defining a new matrix $A(i_1, i_2)$ initialized at 0. When the inversely mapped image pixels are inside the considered region at the source plane we add an area of size 1 to the pixel of the source plane $A(i_1, i_2) = A(i_1, i_2) + 1$, and if the ray falls outside the matrix, we simply ignore it. The representation of this matrix is known as the magnification map.

3.3 Used lens mass distributions

The basic lens equations that are going to be used in this TFM are the following:

- Point mass:
$$\vec{y} = \vec{x} - \frac{\vec{x} - \vec{x_0}}{(\vec{x} - \vec{x_0})^2} \tag{14}$$

- Point mass plus Quadrupolar Perturbation:
$$\vec{y} = \begin{pmatrix} 1 - \kappa_s - \gamma & 0 \\ 0 & 1 - \kappa_s + \gamma \end{pmatrix} \vec{x} - \frac{\vec{x} - \vec{x_0}}{(\vec{x} - \vec{x_0})^2} \tag{15}$$

- SIS (Singular Isotherm Sphere):
$$\vec{y} = \vec{x} - \frac{\vec{x} - \vec{x_0}}{\mid \vec{x} - \vec{x_0} \mid} \tag{16}$$

- SIS plus QP:
$$\vec{y} = \begin{pmatrix} 1 - \kappa_s - \gamma & 0 \\ 0 & 1 - \kappa_s + \gamma \end{pmatrix} \vec{x} - \frac{\vec{x} - \vec{x_0}}{\mid \vec{x} - \vec{x_0} \mid} \tag{17}$$

- Gaussian lens:
$$\vec{y} = \begin{pmatrix} 1 - \kappa_s - \gamma & 0 \\ 0 & 1 - \kappa_s + \gamma \end{pmatrix} \vec{x} - \frac{\vec{x} - \vec{x_0}}{(\vec{x} - \vec{x_0})^2} erf\left(\frac{\vec{x} - \vec{x_0}}{\sqrt{2}\sigma\xi_0}\right) \tag{18}$$

The point lens represents a point of mass, is a fully theoretical construct where all the mass is concentrated at a single point in space. On the other hand a SIS considers a mass distribution where the density of matter decreases linearly with distance from the center of the sphere.

Additionally the quadrupolar perturbation takes into account two terms: the smooth matter convergence κ_s that allows to consider an additional local superficial density of the mass (which may represent smooth DM), and the gravitational shear γ which measures the separation of the mass distribution from the axial symmetry. Note that the total convergence κ depends on the smooth matter convergence κ_s and the stars convergence κ_*, which depends on the fraction of the stars in a surface, so $\kappa = \kappa_* + \kappa_s$.

Thus, in addition to these basic equations we have also considered a system with N particles (N_{bh} or N_{sh} Gaussian lenses). These are given by κ_*.

$$N_{bh} = \frac{\kappa_*}{\pi} \frac{(2x_l)^2}{M_{bh}} \tag{19}$$

Therefore, the mean magnification produced by a lens distribution depends on the total convergence κ and the shear γ.

$$< \mu > = \frac{1}{(1 - \kappa - \gamma)(1 - \kappa + \gamma)} \tag{20}$$

This equation (Eq. 20) is going to be very useful to analyze our results.

3.4 Nearest Neighbours Algorithm

When we shot a 'ray' from the image plane it hits a given position at the source plane that is then discretized to the limits of a pixel size causing noise. To reduce this noise we can diminish the pixel size and increase the number of pixels, which is computationally expensive. A 'cheaper' strategy to reduce noise is to apportioning the ray between the neighbouring pixels (nearest neighbours algorithm).

Here is how it works: as it was explained before, with each iteration we identify the pixel that is inside the source $(I(j_1, j_2) = F(i_1, i_2))$, then the algorithm identifies the nearest known pixels; right, above, and diagonally upper-right and assigning each of these four pixels a corresponding section of the area of size 1 (instead of $A(i_1, i_2) = A(i_1, i_2) + 1$). This approach helps to reduce the noise, resulting in a more smooth magnification map. An example of the improvement of the use of the nearest neighbours algorithm and its comparison without using it is shown at Figure 3:
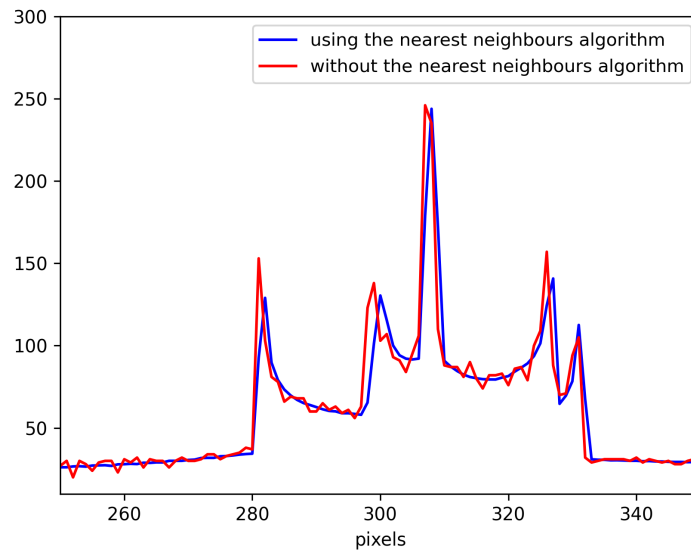
Figure 3: Comparison between a magnification map slice using the nearest neighbours algorithm and not using it. It can be seen that the curve is very much smoother for the nearest neighbours algorithm.

The Figure 3, presents a slice of the same magnification map done with the nearest neighbours algorithm and the original one, it can be seen that it is smoother than the one made without it.

3.5 Python and FORTRAN codes

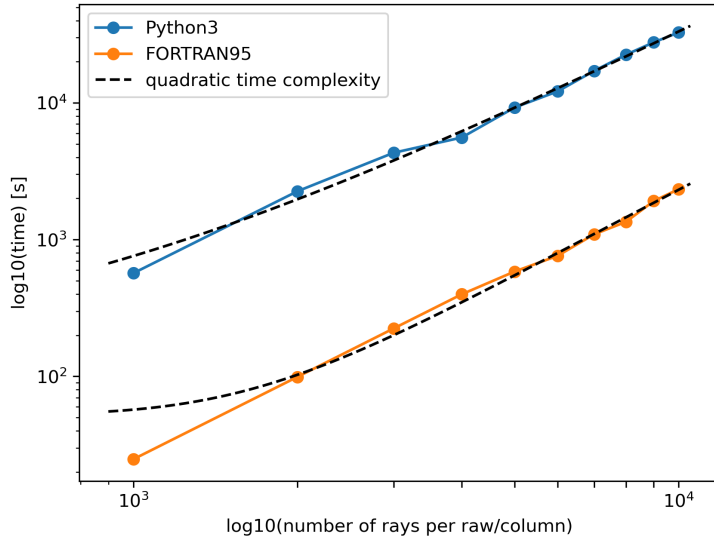Fortran95 has demonstrated significantly higher efficiency compared to Python3 (see Figure: 4).

Figure 4: Execution time comparison for the same random uniform distribution map with 200 point lenses (Eq. 15), considering different number of rays (nx) for Python3 and FORTRAN95. Notice that the time execution dependency is quadratic with the number of rays.

Figure 4 shows a quadratic dependence between the number of rays and the execution time. This behavior is expected, since the inverse ray shooting algorithm employs a double loop that depends on nx. This Figure also shows that by changing the code from Python3 to FORTRAN95 we will achieve a considerable time reduction, by a factor of 17 in average.

3.6 Use of online IPM code

Even with the use of the Nearest Neighbours algorithm in Fortran95 our code has its limits, and as it is necessary to do massive simulations, we need to make use of more advanced algorithms. That is why it is going to be used the code based in Inverse Polygon Method described by [3] that can be executed at the internet address: https://gloton.ugr.es/microlensing/.

The program works as follows:

- **Select parameters of the simulation**: such as convergence (κ), smooth matter convergence (κ_s), shear (γ), minimum and maximum mass of the lenses, map size (yl) and number of pixels (ny).

- **Generate the distribution of millilenses**: There are two options; the program can generate a random uniform distribution of point masses, or a distribution previously created by us can be uploaded.

- **Generate magnification map and histogram**: When everything is ready, the simulation can start and it would produce a magnification map and its histogram, then we download our magnification file data produced by the program to later make our averaged histogram.

For a random uniform distribution of BH's, the program will be left to create this distribution of BH's, meanwhile for a clustered distribution of BH's, these can not be generated by the program, so the spatial distribution of BH's would be generated by us.

The computational efficiency is very important in this TFM, as we need to do a large number of magnification maps, as the PDF's are very sensible to sample variance. We have done thousands of realizations of which we have used 553 of them.

4 Results and Discussion

4.1 Clustered BH's

4.1.1 Magnification probabilities for a population of random uniformly distributed BH's

As previously mentioned, published studies [1] indicate that DM are unlikely to consist in PBH's, however they do not contemplate a clustered distribution of PBH's. This clustered distribution should generate flux-ratio anomalies in the images of lensed quasars images similar to the ones observed, to be considered a viable alternative to explain DM.

4.1.1.1 Comparison with the theoretical result in the sparse case

In order to check that our results are consistent, it is convenient to compare our simulations with the theoretical predictions available for the sparse case. We are going to do this through the study of the magnification probability density function, $PDF(\mu)$. These are defined as the normalized histogram of the magnification. Therefore, it represents the likelihood of a given magnification to be produced by a given lens distribution. A distribution of micro/millilenses is considered sparse when in a region of several Einstein radii around each microlens the deflection of the light rays depends only marginally on the rest of the microlenses [9]. From [9] the $PDF(\mu)$ of the sparse case is given by the function:

$$PDF(\mu) = \frac{2 < \mu > \kappa}{(\mu^2 - 1)^{3/2}}. \tag{21}$$

Then we simulate 50 magnification maps considering a relatively low mass density: $\kappa_* = 0.1$, $\kappa_s = 0$, $\gamma = 0$, $yl = 25ER$, $ny = 2000$, a minimum mass of 0.999 and a maximum mass of 1.001. The theoretical magnification for these parameters is 1.2345 mag (Eq. 20). An example of this type of map is presented in Figure 5:
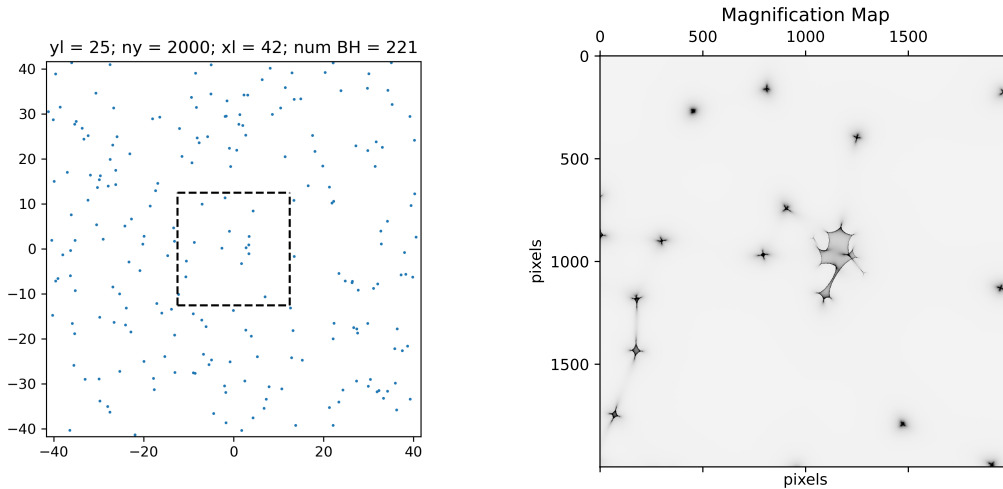
(a) Random uniform distribution of BH's; the mapped region is enclosed by the black dashed lines.

(b) Magnification map of the random uniform distribution of BH's shown in Figure 5a.

Figure 5: Random uniform distribution of BH's with its magnification map considering $\kappa_* = 0.1$, $\kappa_s = 0$, $\gamma = 0$, $yl = 25ER$, $ny = 2000$, a minimum mass of 0.999 and a maximum mass of 1.001.

The Figure 5 shows that the distribution is not perfectly sparse, because of the presence of caustics, since we are considering a distribution of point lenses.

Averaging the PDF's of 50 different magnification maps to reduce sample variance, which were obtained using the IPM algorithm, the comparison with the sparse case function (Eq. 21) can be done (see Figure 6).
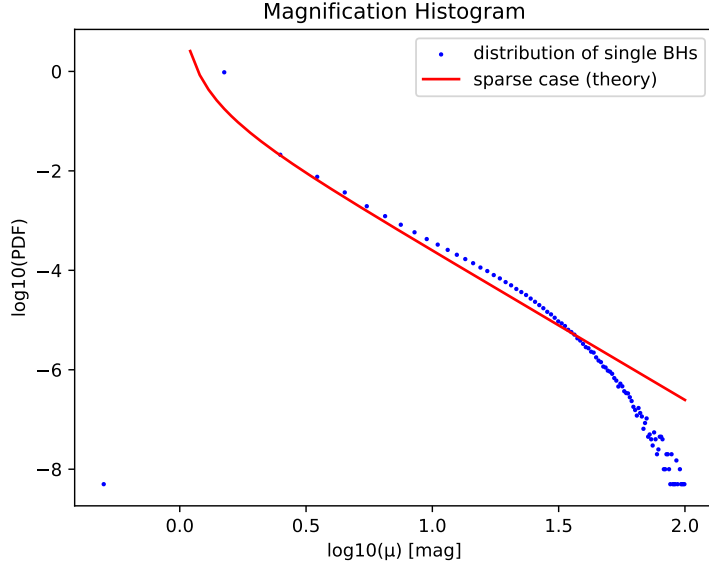
Figure 6: Average PDF obtained from 50 magnification maps for the case $\kappa_* = 0.1$, $\kappa_s = 0$, $\gamma = 0$, $yl = 25ER$, $ny = 2000$, a minimum mass of 0.999 and a maximum mass of 1.001, compared with the function for the sparse case (Eq. 21).

Figure 6 is a verification of our simulation procedure. There is a bump excess between $0.5 < log10(\mu) < 1.5$, due to the caustic contribution, produced by the combined action of two or more microlenses on the light rays, which is not taken into account in the theoretical prediction (Eq. 21). On the other hand for $log10(\mu) > 1.5$ appears a deviation from the μ^{-3} theoretical law, because of the limited resolution (pixelsize) that smooths the magnification map.

4.1.1.2 Magnification maps and PDF's

The objective of this TFM is to study the effect of clustering on the magnification induced in a lensed quasar by a population of compact objects in the lens galaxy, so the natural basis to start is to study a non-clustered random uniform distribution of BH's specifically in order to illustrate the effects of clustering, we will start comparing the results obtained from a random uniform distribution of BH's, and a clustered case with the same number of BH's, with clusters of $R_{cluster} = 4ER$ and 40 BH's per cluster.

In Figures 7 and 8 we compare the distribution of BH's in both cases and the magnification maps, respectively. The most interesting result of the comparison between magnification maps is the scale of the caustic structure, which is very much larger for the clustered BH's. As we will see in section 4.1.2.1 this reflects that clusters act like giant pseudo-particles.
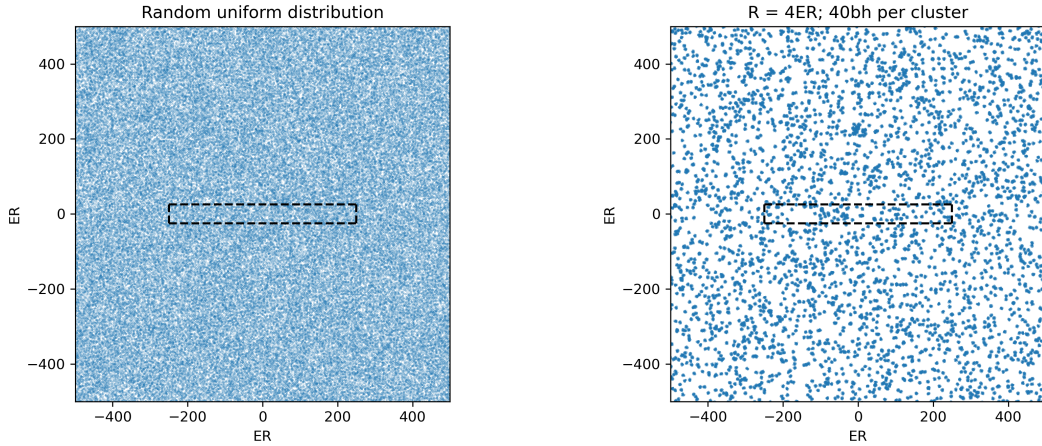
(a) Random uniform distribution of BH's.

(b) Clustered distribution of BH's, with clusters of $R_{cluster} = 4ER$ and 40 BH per cluster.

Figure 7: Comparison between a random uniform distribution of BH's and a clustered case with clusters of $R_{cluster} = 4ER$ and 40 BH per cluster. Considering for both cases: $y_l = 50ER$, $ny = 1000$, $\gamma = 0.45$, $\kappa_* = 0.45$, $\kappa_s = 0.0$ a minimum mass of 0.999 and a maximum mass of 1.001.
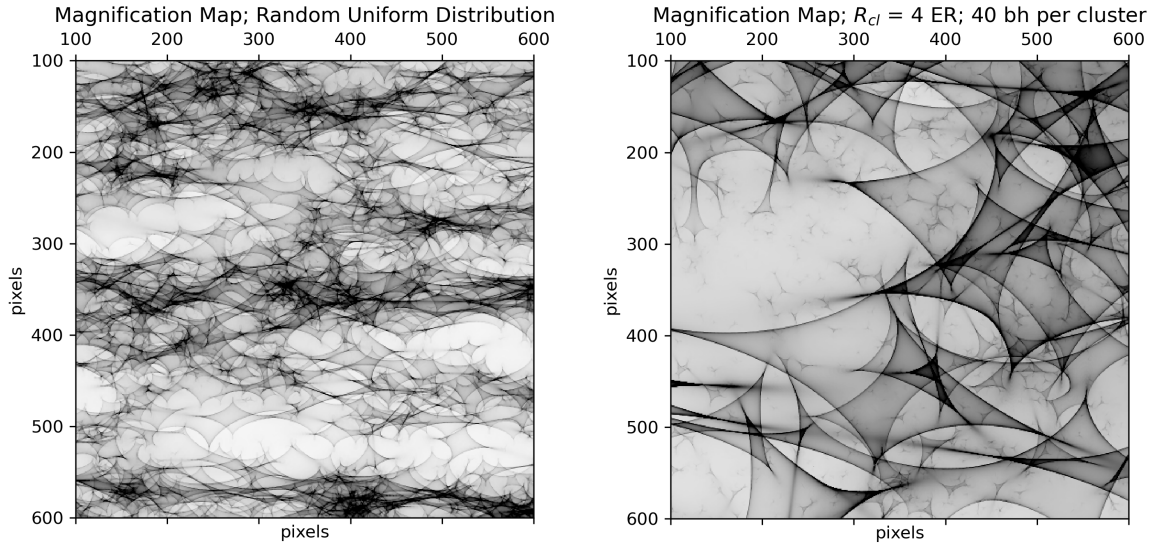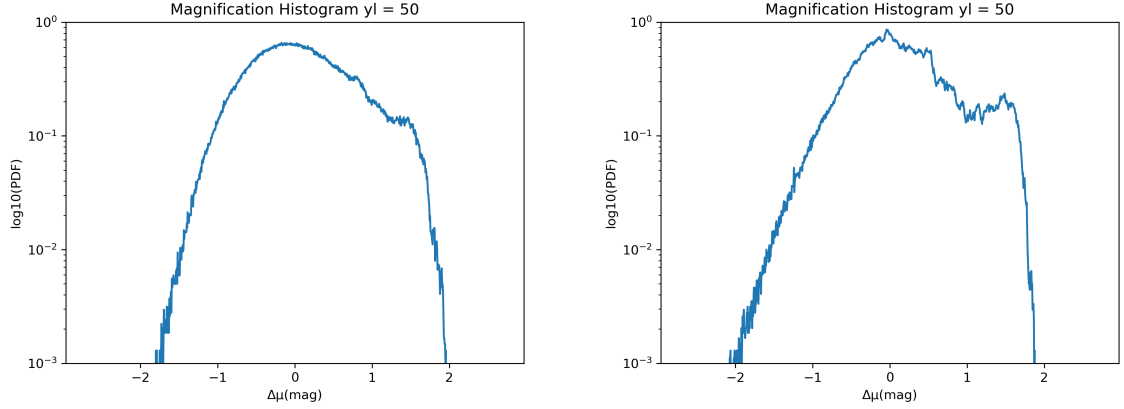

(a) Magnification map of a random uniform distribution of BH's.

(b) Magnification map of a clustered distribution of BH's, with clusters of $R_{cluster} = 4ER$ and 40 BH per cluster.

Figure 8: Magnification map of a random uniform distribution of BH's and a clustered distribution of BH's, with clusters of $R_{cluster} = 4ER$ and 40 BH per cluster.

In Figure 8 we can see that the uniform distribution has a unique scale for the caustics, while the clustered distribution has caustics with a large scale produced by the clusters action, previously mentioned, and caustics with a small scale produced by single BH's.

In Figure 9 we show the corresponding normalized magnification histograms. Notice that the one associated to the clustered BH's appears much more irregular. This is a consequence of clustering. As we will see in section 4.1.2.1 clusters act like giant pseudo-particles and, hence clustering result in a decrease of the number of effective particles with a consequent increase of the impact of fluctuations

related to sample variance.

(a) Magnification histogram of a random uniform distribution of BH's and clustered distribution of BH's.

(b) Magnification histogram of a clustered distribution of BH's, with clusters of $R_{cluster} = 4ER$ and 40 BH per cluster.

Figure 9: In Figure 9 we show the corresponding normalized magnification histograms. Notice that the one associated to the clustered BH's appears much more irregular.

As we can see from the Figure 9 the individual maps are truly erratic due to the random distribution of both clusters and BH's, as a consequence we need to do several realizations for each case in order to reduce the sample variance. Thus, we will average 50 magnification maps for each case. In Figure 10 we show the results of averaging in the case of the random uniformly distributed BH's.
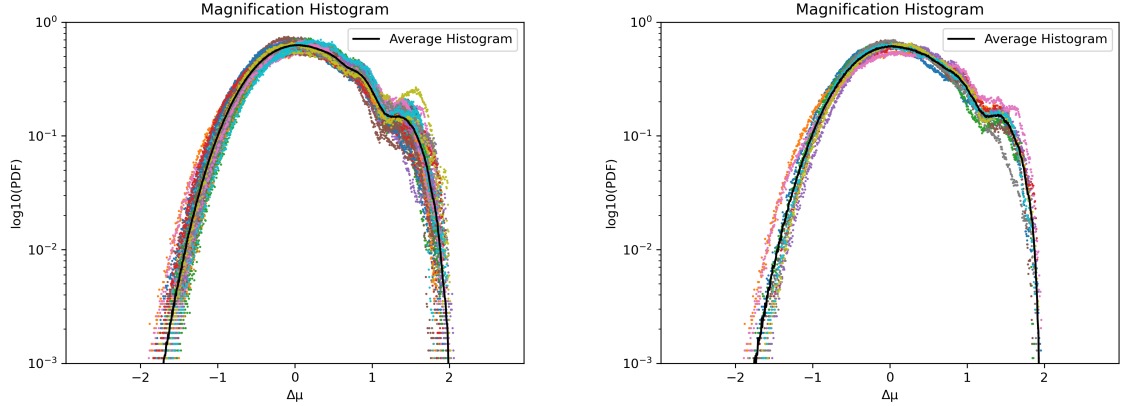
(a) Average magnification histogram for a population of random uniformly distributed BH's, and the 50 single realizations of magnification histograms.

(b) Average magnification histogram for a population of random uniformly distributed BH's. To make easier the visualization, in this plot we present only 10 of the single realizations of the single realizations.

Figure 10: Average magnification histogram for a population of random uniformly distributed BH's, considering $y_l = 50ER$, $ny = 1000$, $\gamma = 0.45$, $\kappa_* = 0.45$, $\kappa_s = 0.0$ a minimum mass of 0.999 and a maximum mass of 1.001.

In Figure 11 we show the results of averaging for the clustered distribution of BH's, with clusters of $R_{cluster} = 4ER$ and 40 BH per cluster.
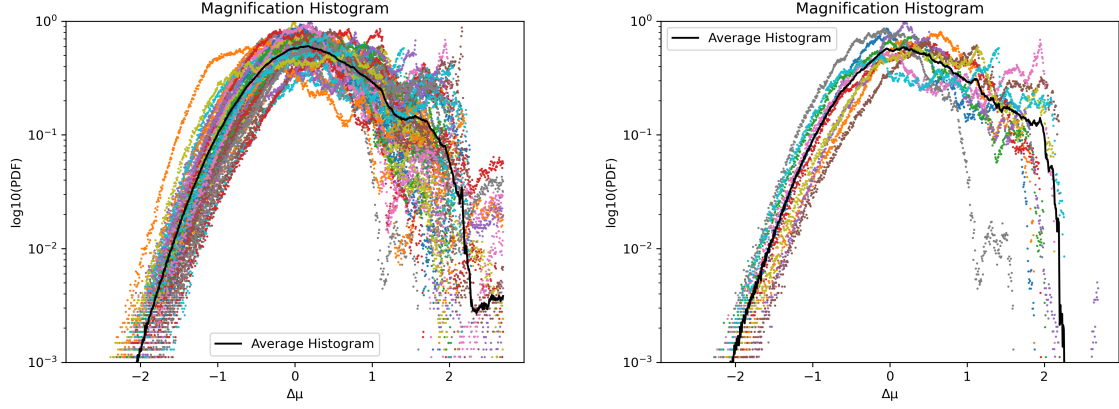
14

(a) Average magnification histogram for a population of clusters with $R_{cluster} = 4ER$ and 40 bh per cluster, and the 50 included magnification histograms.

(b) Average magnification histogram for a population of clusters with $R_{cluster} = 4ER$ and 40 bh per cluster. To make easier the visualization, in this plot we present only 10 of the included PDF's.

Figure 11: Average magnification histogram for a population of clusters with $R_{cluster} = 4ER$ and 40 bh per cluster, considering $y_l = 50ER$, $ny = 1000$, $\gamma = 0.45$, $\kappa_* = 0.45$, $\kappa_s = 0.0$ a minimum mass of 0.999 and a maximum mass of 1.001.

$\Delta\mu$ is defined as the change of magnification produced by the lenses, defining the difference in flux between the source lensed and unlensed,

$$\Delta\mu = -2.5log\left(\frac{\mu}{<\mu>}\right). \tag{22}$$

Hereafter, we will average the histograms of 50 magnification maps to mitigate sample variance (like in Figure 10).

### 4.1.2 Magnification probabilities for clustered BH's.

In this section we are going to study the clustering of BH's and its effects on magnification statistics. Our first aim is to analyze to what extent a compact cluster is analogous to a single point object.

The second objective is to analyze how the magnification statistics changes depending on the clumpiness of the cluster. We have decided to maintain a constant size for the clusters $R_{cluster} = 4ER$ and varying the number of BH's per cluster.

4.1.2.1 Small and large scales: pseudo-particles limit

We are going to study to what extent at large scales a compact cluster behaves as a pseudo-particle and is in practice indistinguishable from a single compact object of the same mass than the cluster.

To check this hypothesis we have considered a random uniform distribution of BH's with mass 80, and located at the same places two distribution of clusters with 80 BH's of 1 mass one of them with $R_{cluster} = 1ER$ and another clustered distribution with $R_{cluster} = 5ER$. See Figure 12.
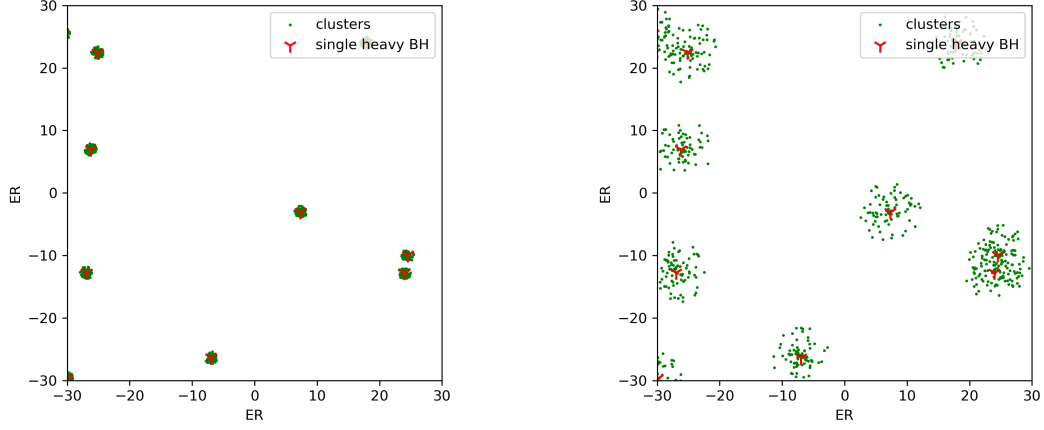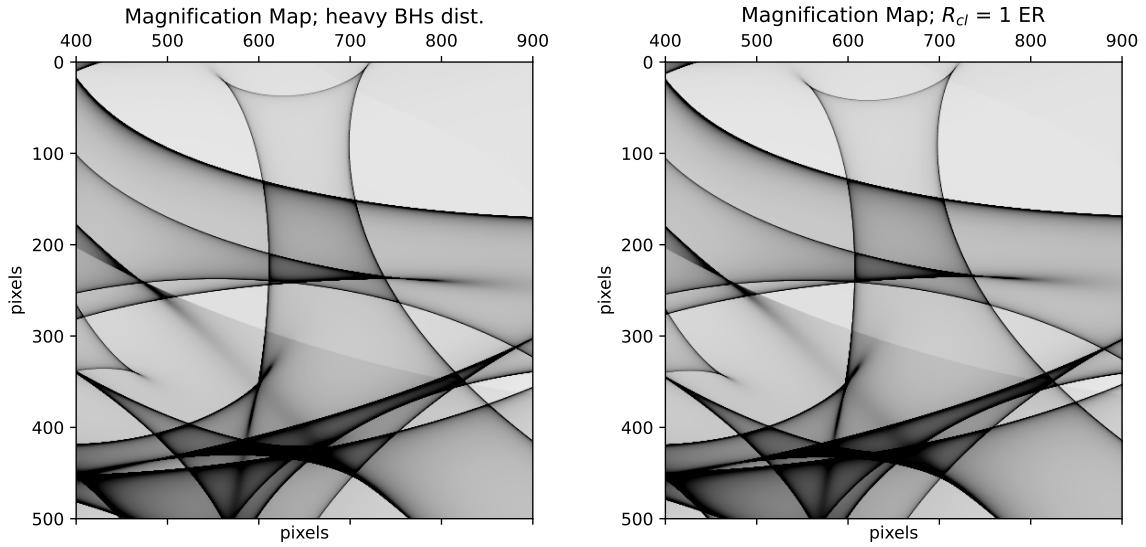
(a) Distributions of 1007 clusters with 80 BH's and $R_{cluster} = 1ER$ (green points) and the random uniform distribution of BH's with 80 mass (red points).

(b) Distributions of 1007 clusters with 80 BH's and $R_{cluster} = 5ER$ (green points) and the random uniform distribution of BH's with 80 mass (red points).

Figure 12: Comparison between the random uniform distribution of BH's with mass 80 and the clusters (located in the same places) with 80 BH's with 1 mass and radii $1ER$ and $5ER$.

In Figures 13 and 14 we show the corresponding magnification maps and $PDF(\mu)$ histograms corresponding to the cases of the uniform distribution of BH's with mass 80 and the clustered case with $R_{cluster} = 1ER$.

(a) Magnification Map of a distribution of BH's with masses 80.

(b) Magnification Map of a distribution of cluster of 1ER with 80 BH's per cluster.

Figure 13: Comparison of magnification maps between the case of a distribution of 1007 BH's with mass 80 and the magnification map of the same distribution of 1007 cluster of 1ER with 80BH's per cluster.

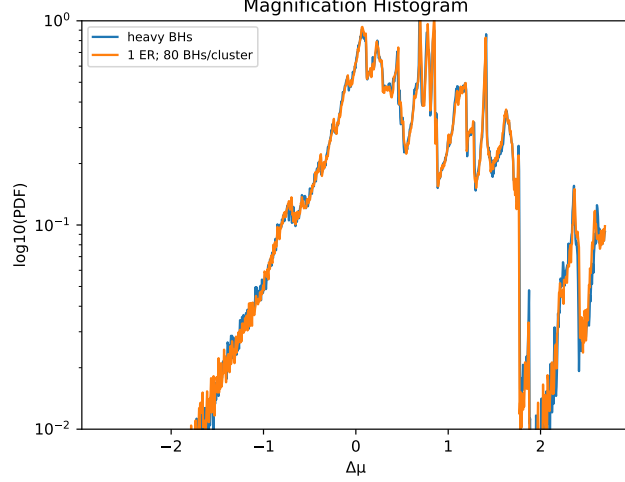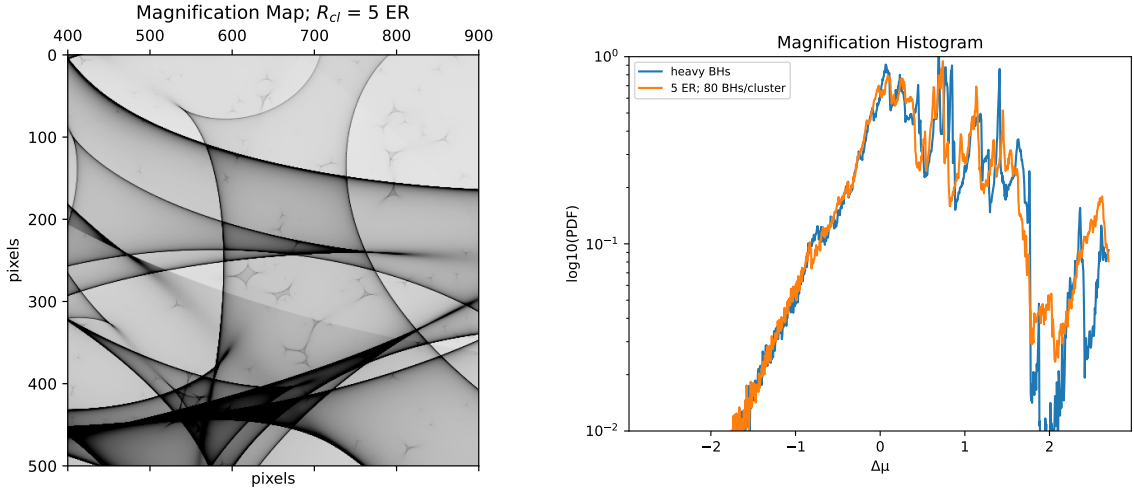In Figure 13 we can see that the magnification maps of both cases are virtually indistinguishable.

Figure 14: Magnification histogram of 1007 clusters with 80 BH's and $1ER$ case and the single BH's with a mass of 80 case.

In Figure 14 we can see that the PDF's of both distributions are very similar. This implies that the large scale structure corresponding to the clusters acting as giant pseudo-particles is ruling the magnification statistics.

In Figure 15 we can see the magnification map for the $R_{cluster} = 5ER$ case and the $PDF(\mu)$ histograms corresponding to the cases of the uniform distribution of BH's with mass 80 and the clustered case with $R_{cluster} = 5ER$.

(a) Magnification Map of a distribution of cluster of 5ER with 80 BH's per cluster.

(b) Magnification histogram of 1007 clusters with 80 BH's and $5ER$ case and the single BH's with a mass of 80 case.

Figure 15: Magnification Map and histogram obtained from the clustered distribution of 1007 clusters with 80 BH's and $R_{cluster} = 5ER$ case (Figure 12b).

As we can see in Figures 15a and 13a, the magnification map of both cases are very similar although in the map of the clustering case with $R_{cluster} = 5ER$ (Figure 15a), we can see that the pattern of the large caustics is different, as they are more separated, and we can see small caustics generated by the single 1 mass BH's. These differences are almost not appreciable when the comparison is made with the clustering of $R_{cluster} = 1ER$ (see Figure 13b).

4.1.2.2   Constant size, variable number of BH's

We are going to study the PDF's produced by clusters distributions with the same size and different number of BH's per cluster. We have shown some of the results in section 4.1.1.2, so considering $y_l = 50ER$, $ny = 1000$, $\gamma = 0.45$, $\kappa_* = 0.45$, $\kappa_s = 0.0$ a minimum mass of 0.999 and a maximum mass of 1.001. The theoretical magnification for these parameters is 10.0 mag (Eq. 20).

In Figure 16 we can see the $PDF(\mu)$ histograms corresponding to the cases with the same size ($R_{cluster} = 4ER$) varying the number of BH's per cluster; $10:20:40:80$, compared with the random uniform distribution case.
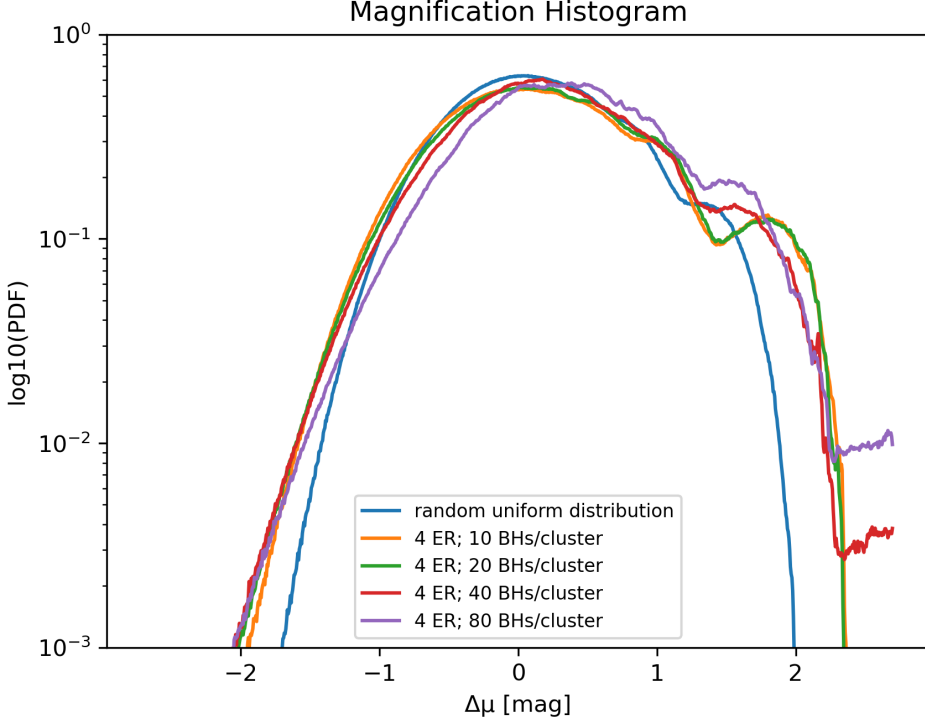

Figure 16: Averaged magnification histogram of 50 maps, each with a constant size of $R_{cluster} = 4ER$ and varying numbers of BH's per cluster: 10 bh (orange) with a mean magnification of 10.02 mag, 20 bh (green) with a mean magnification of 9.74 mag, 40 bh (red) with a mean magnification of 9.44 mag and 80 bh (purple) with a mean magnification of 8.42 mag, compared with the random uniform distribution (blue) with a mean magnification of 9.94 mag.

As we can see in Figure 16, the probabilities of large magnifications increases with compactness.

Furthermore, with the decrease of the number of BH's per cluster, the shape of the histograms tends to be narrower being the random uniform distribution of BH's their limit.

It can be noticed that the mean magnification decreases with compactness, this seems to be odd since the theoretical mean magnification depends in the convergence κ and the shear γ. Nevertheless, since we are working with clusters that behave like pseudo-particles of mass the sum of the masses of the individuals BH's, the number of pseudo-particles per magnification map will be relatively small and, consequently, the spatial cluster distribution will be significantly affected by random fluctuations. This can be partially solved by increasing the map size (and hence the number of clusters) of lenses and averaging 50 magnification maps so that we mitigate the impact of sample variance, explained in section 4.1.1.2. However, it is impossible to have an infinite number of pseudo-particles, and this is a limit in our simulations, since clusters inside the mapping region bend rays coming from the outside inward, while clusters outside the mapping region divert the rays inward, so if the number of clusters were infinite, then the rays from outside and inside would compensate, but since we are limited, we

will have a deficit in the rays that enter the mapping region, and therefore the mean magnification will be in the average less than the theoretical magnification.

4.1.3 Bayesian Analysis

The Bayes theorem is given by the expression:

$$P(A|B) = \frac{P(B|A)P(A)}{P(B)} \tag{23}$$

Where $P(A|B)$ is posterior probability of A given B, $P(B|A)$ is the conditional probability of B given A and $P(A)$ and $P(B)$ are the unconditional probabilities of A and B.

In the context of this TFM we want to estimate the probability of a given compactness, for an observed magnification, $P(compactness|\Delta\mu)$, so applying the Bayes theorem:

$$P(compactness|\Delta\mu) \propto P(\Delta\mu|compactness)P(compactness). \tag{24}$$

We obtain $P(\Delta\mu|compactness)$ from our simulations (in Figure 16) and we consider a uniform probability for $P(compactness)$.

4.1.3.1 Observed millilensing

Comparing the flux ratios between the images of quadruply lensed quasars with 4 images predicted by lens models based in the positions of the images with the observed flux-ratios, Heydenreich et al. 2024 [10] obtain a mean anomaly (i.e. a difference between the model and the observations) of $|\Delta\mu| = 0.27 \pm 0.1$ mag.

4.1.3.2 Bayesian Analysis

The Figure 17 shows the 2D PDF depending on the compactness and the magnification, for the case of clusters with constant size, $R_{cluster} = 4ER$. From the simulated data obtained in Figure 16.
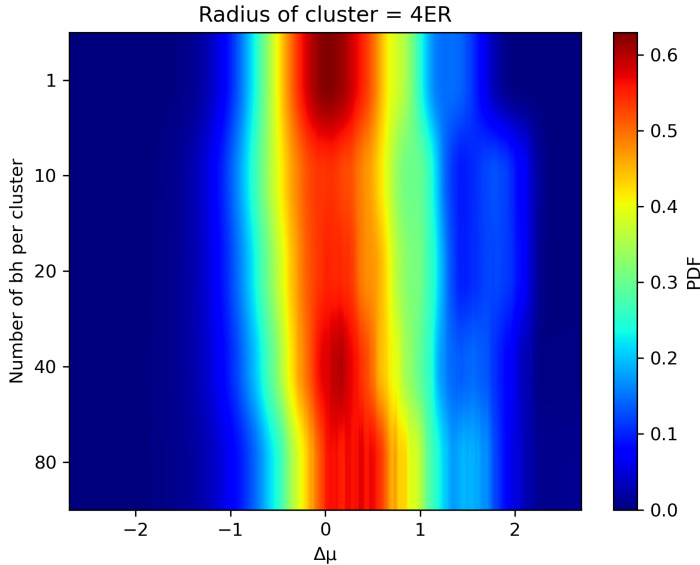

Figure 17: 2D PDF depending on the number of BH per cluster and the magnification, considering clusters with $R_{cluster} = 4ER$.

Figure 18 shows the probability of different magnifications ($\Delta\mu = -1. : -0.5 : -0.25$ mag) depending on the size and the number of BH's per cluster.
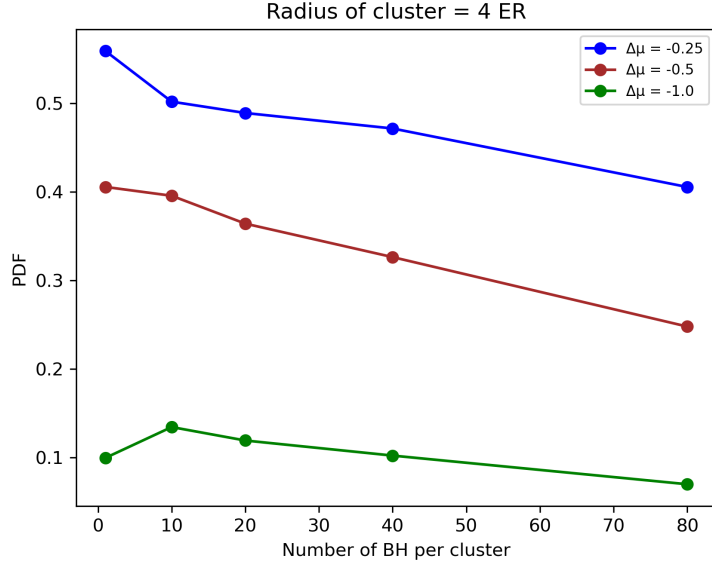
Figure 18: Probability density functions $PDF(\mu)$ vs number of BH's per cluster, for the different microlensing magnifications, considering clusters with $R_{cluster} = 4ER$.

As the mean measured anomalies are about 0.27 mag. We can conclude from Figures 17 and 18 that the uniform distribution has more probability to generate the observed magnification anomalies than the clustered distributions. Notice that to favour the clustering hypothesis the observed magnifications should be as large as -1 mag.

4.2 Gaussian subhaloes

As pointed out in the Introduction, simulation of structure formation show that galactic haloes could contain haloes of much lower mass, the subhaloes. In this section we are going to study these subhaloes and their effect in the magnification map and the $PDF(\mu)$. To simplify this study we are going to consider that these subhaloes have a Gaussian radial mass profile.

The lensing equation for this Gaussian subhaloes corresponds to (Eq. 18), where ξ_0 is the Einstein radius of the subhalo. In order to work in Einstein radii units we will consider $\xi_0 = 1ER$.

4.2.1 Magnification probabilities for a population of Gaussian subhaloes

In this part of the section we are going to compare the magnification probability density functions, $PDF(\mu)$ for different subhaloes of compactness $\sigma = 0.01\xi_0 : 1\xi_0 : 2\xi_0 : 4\xi_0$ and the point lens. This subhaloes are supposed to be distributed sparsely, so the considered parameters for the simulations are $yl = 60ER$, $ny = 1000$, $\gamma = 0.0$, $\kappa_* = 0.1$, $\kappa_s = 0.0$. The theoretical magnification for these parameters is 1.2345 mag (Eq. 20).

In Figure 19 we show an example of the random uniform distribution of Gaussian subhaloes.
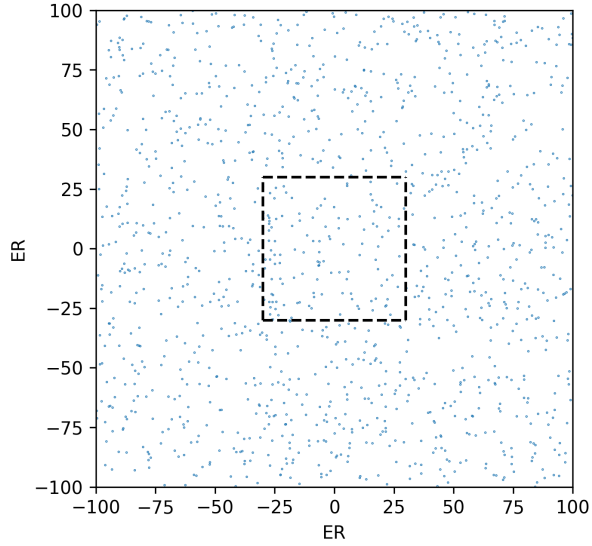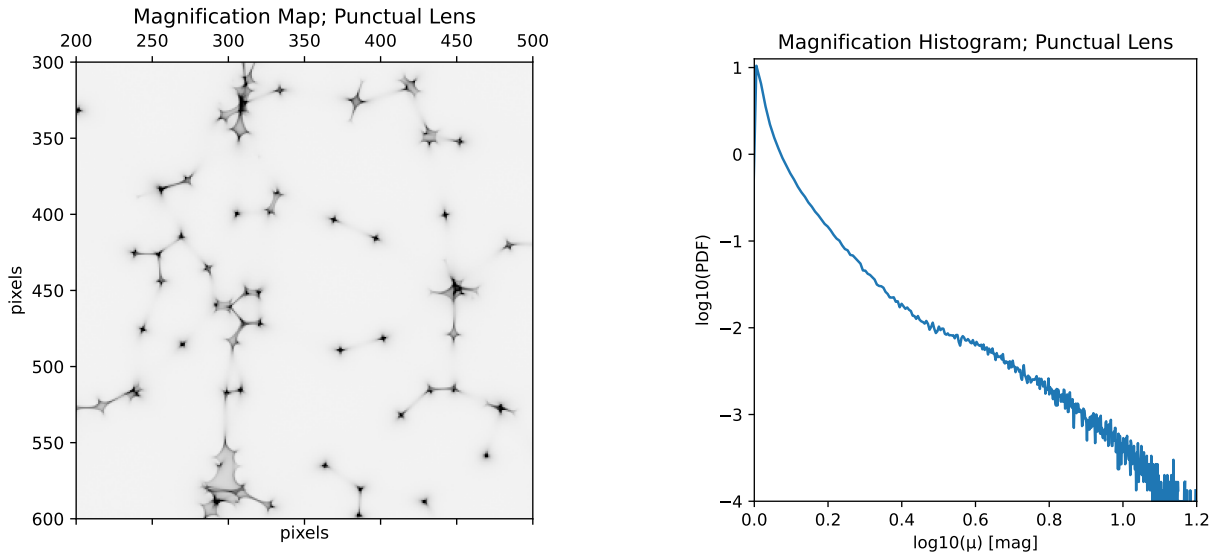
Figure 19: Distribution of subhaloes, considering the parameters; $yl = 60ER$, $ny = 1000$, $\gamma = 0.0$, $\kappa_* = 0.1$, $\kappa_s = 0.0$.

In Figure 20 we show the magnification map and the histogram corresponding to the random uniform distribution of Figure 19 considering the lenses to be punctual.
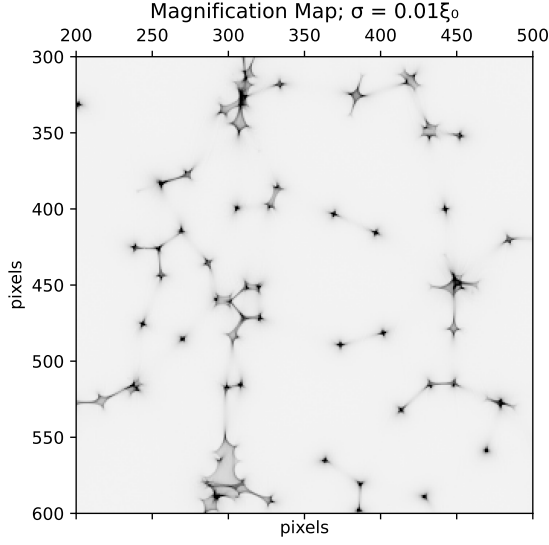

(a) Magnification map of a random uniform distribution of point lenses.
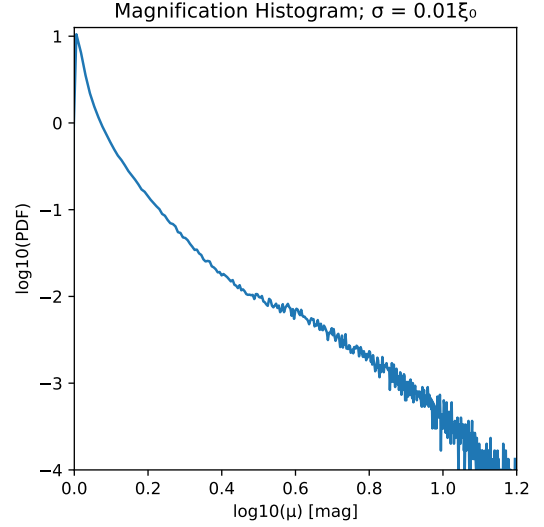

(b) Magnification histogram of a random uniform distribution of point lenses.

Figure 20: Magnification map and histogram of the distribution from Figure 19 using point lenses, considering; $yl = 60ER$, $ny = 1000$, $\gamma = 0.0$, $\kappa_* = 0.1$, $\kappa_s = 0.0$. The mean magnification is 1.2317 mag.

In Figure 21 we show the magnification map and the histogram of the random uniform distribution of Figure 19 considering the lenses to be Gaussian subhaloes with $\sigma = 0.01\xi_0$.
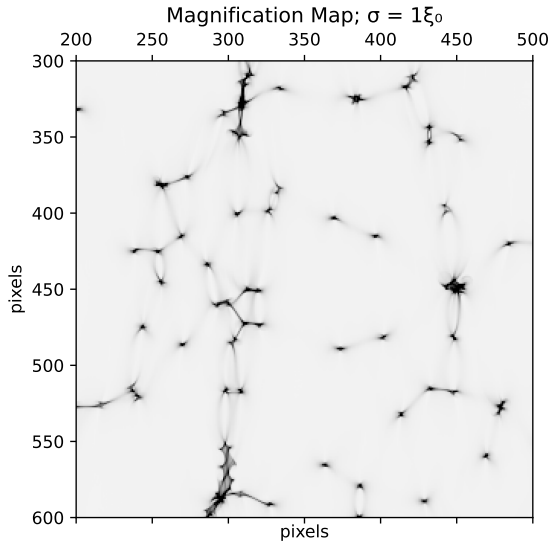
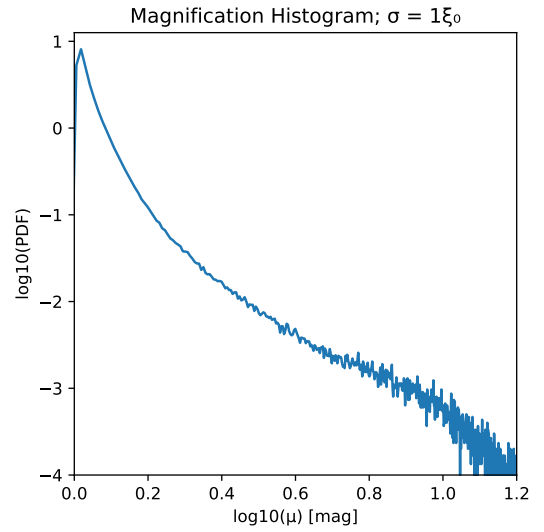(a) Magnification map of a random uniform distribution of Gaussian subhaloes with $\sigma = 0.01\xi_0$.

(b) Magnification histogram of a random uniform distribution of Gaussian subhaloes with $\sigma = 0.01\xi_0$.

Figure 21: Magnification map and histogram of the distribution from Figure 19 using Gaussian subhaloes with $\sigma = 0.01\xi_0$, considering; $yl = 60ER$, $ny = 1000$, $\gamma = 0.0$, $\kappa_* = 0.1$, $\kappa_s = 0.0$. The mean magnification is 1.2317 mag.

In Figure 22 we show the magnification map and the histogram of the random uniform distribution of Figure 19 considering the lenses to be Gaussian subhaloes with $\sigma = 1\xi_0$.
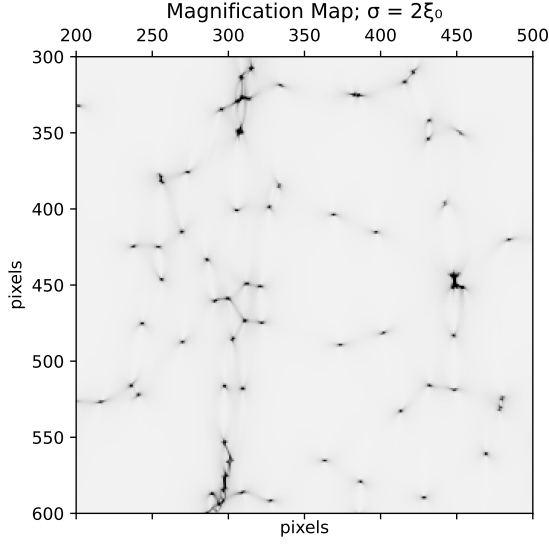

(a) Magnification map of a random uniform distribution of Gaussian subhaloes with $\sigma = 1\xi_0$.
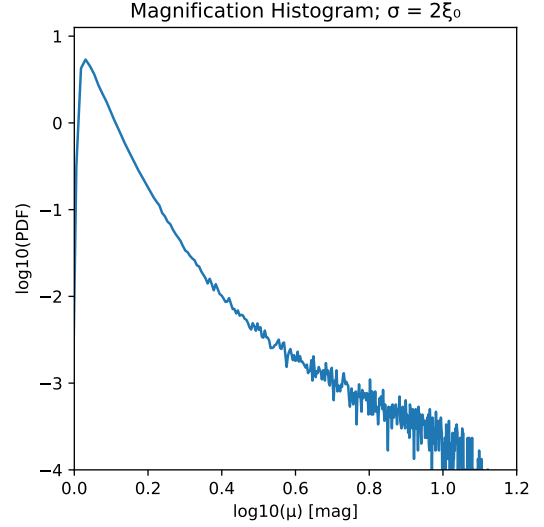
(b) Magnification histogram of a random uniform distribution of Gaussian subhaloes with $\sigma = 1\xi_0$.

Figure 22: Magnification map and histogram of the distribution from Figure 19 using Gaussian subhaloes with $\sigma = 1\xi_0$, considering; $yl = 60ER$, $ny = 1000$, $\gamma = 0.0$, $\kappa_* = 0.1$, $\kappa_s = 0.0$. The mean magnification is 1.2303 mag.

In Figure 23 we show the magnification map and the histogram of the random uniform distribution of Figure 19 considering the lenses to be Gaussian subhaloes with $\sigma = 2\xi_0$.

Magnification Map; σ = 2ξ₀

Magnification Histogram; σ = 2ξ₀

(a) Magnification map of a random uniform distribution of Gaussian subhaloes with $\sigma = 2\xi_0$.

(b) Magnification histogram of a random uniform distribution of Gaussian subhaloes with $\sigma = 2\xi_0$.

Figure 23: Magnification map and histogram of the distribution from Figure 19 using Gaussian subhaloes with $\sigma = 2\xi_0$, considering; $yl = 60ER$, $ny = 1000$, $\gamma = 0.0$, $\kappa_* = 0.1$, $\kappa_s = 0.0$. The mean magnification is 1.2288 mag.

In Figure 24 we show the magnification map and the histogram of the random uniform distribution of Figure 19 considering the lenses to be Gaussian subhaloes with $\sigma = 4\xi_0$.

Magnification Map; σ = 4ξ₀
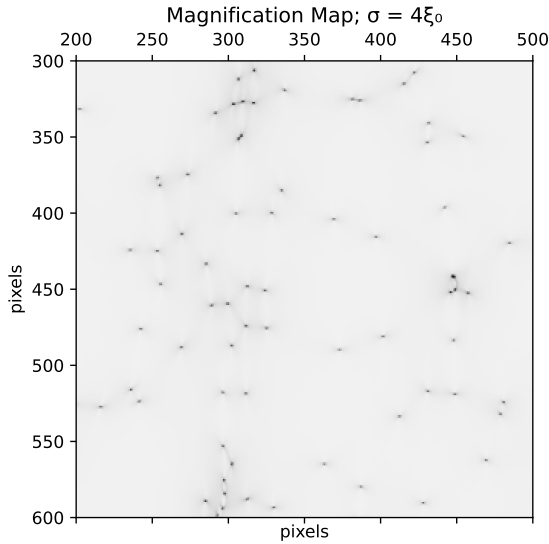
Magnification Histogram; σ = 4ξ₀

(a) Magnification map of a random uniform distribution of Gaussian subhaloes with $\sigma = 4\xi_0$.
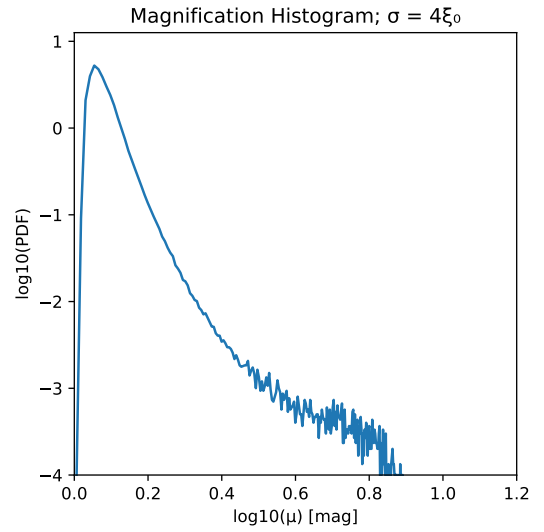
(b) Magnification histogram of a random uniform distribution of Gaussian subhaloes with $\sigma = 4\xi_0$.

Figure 24: Magnification map and histogram of the distribution from Figure 19 using Gaussian subhaloes with $\sigma = 4\xi_0$, considering; $yl = 60ER$, $ny = 1000$, $\gamma = 0.0$, $\kappa_* = 0.1$, $\kappa_s = 0.0$. The mean magnification is 1.2255 mag.

From the different magnification maps, we can see that the caustics tend to disappear with the increase of σ. This implies that the high magnifications are going to be less probable.

The point lens equation (Eq. 15) is a limit case of Gaussian subhalo lens equation (Eq. 18) with an infinite compactness, so in order to cross-check that our simulating results are correct, we are going to compare the case of Gaussians subhaloes with high compactness ($\sigma = 0.01\xi_0$) distribution and the case of point lens distributions. In Figure 25 we show a comparison between the PDF's of these cases.
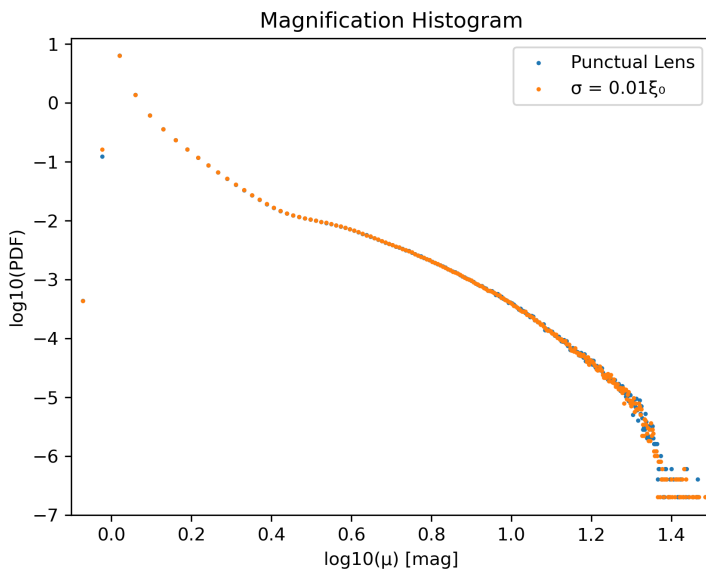
Figure 25: Comparison between the cases of a point lens distribution with a mean magnification of 1.2335 mag, and the case of Gaussians subhaloes with $\sigma = 0.01\xi_0$ with a mean magnification of 1.2335 mag.

Figure 25 shows that the point lens case is a limit case of a Gaussian subhalo with a sufficiently high compactness ($\sigma << 1$).

In Figure 26 we show the $PDF(\mu)$ with different compactness $\sigma = 1\xi_0 : 2\xi_0 : 4\xi_0$ and the point lens case, compared with the theoretical sparse case function (Eq. 21).

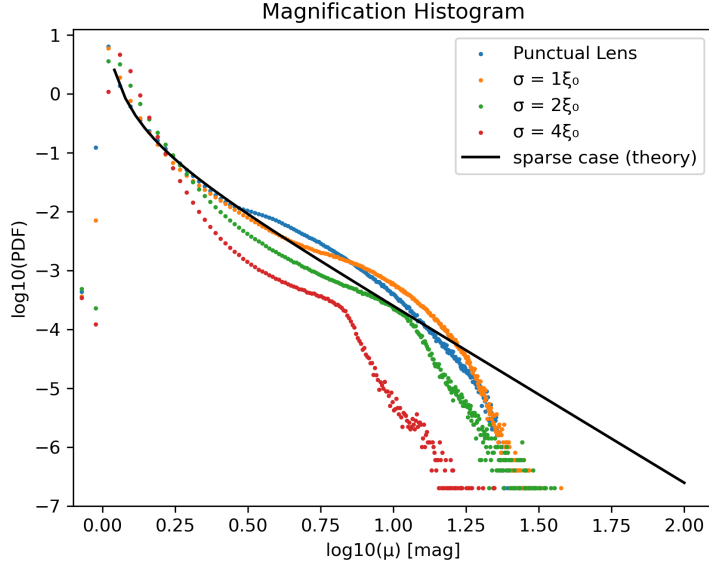Figure 26: Averaged magnification histogram of 50 maps, considering different compactness: $\sigma = 1\xi_0$ (orange dots) with a mean magnification of 1.2319 mag, $\sigma = 2\xi_0$ (green dots) with a mean magnification of 1.2303 mag, $\sigma = 4\xi_0$ (red dots) with a mean magnification of 1.2269 mag, the point lens case (blue dots) with a mean magnification of 1.2335 mag, compared with the function for the sparse case (Eq. 21), from [9].

Figure 26 shows how the different cases of Gaussians subhaloes PDF's behave with different compactness, comparing them with the point lens case and the sparse function (Eq. 21). It shows that the probability of high magnifications increases with compactness. The most compact cases are in a very good agreement with the theoretical sparse case function, and (similarly to the results obtained in Figure 6) there is a bump excess due to the presence of caustics, and there is a decay for the highest values of magnification because of the limited resolution (pixelsize).

4.2.2 Bayesian Analysis

Figure 27 shows the 2D PDF depending on the Gaussian subhaloes compactness and the magnification, These data are taken from Figure 26.
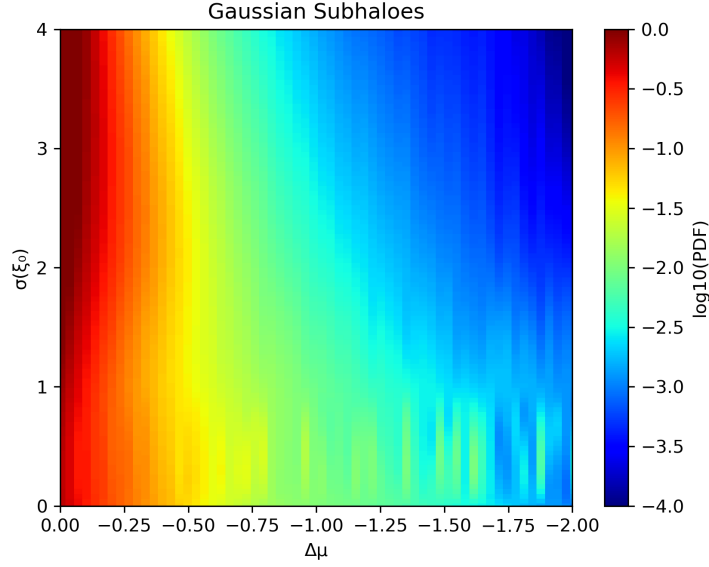
Figure 27: 2D PDF depending on the Gaussian subhaloes compactness and the magnification.

In Figure: 28 we show the probability of different magnifications ($\Delta\mu = -0.1 : -0.2 : -0.3 : -0.4 : -0.5 : -0.6$) depending on the Gaussian subhaloes compactness.
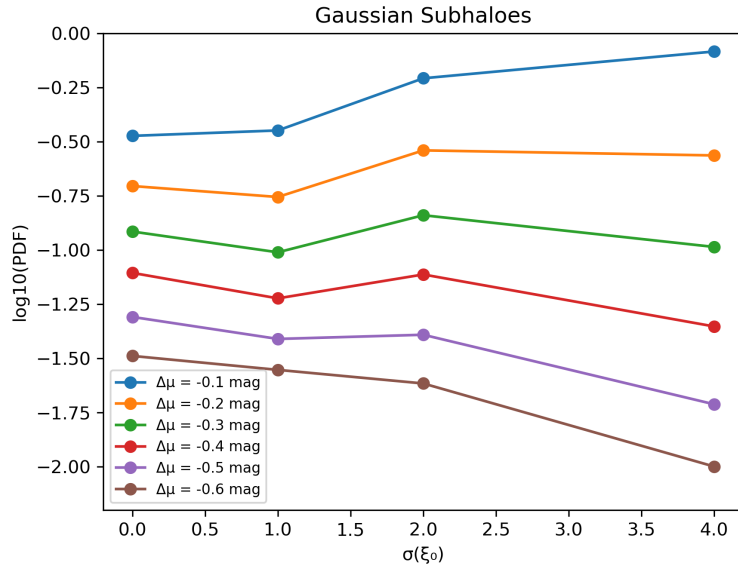
Figure 28: Probability density functions $PDF(\mu)$ vs compactness (σ), for the different microlensing magnifications.

As it can be seen in Figure 28, for relatively small magnifications $\Delta\mu \lesssim 0.3$, the less compact subhaloes are the more likely. On the contrary, for large magnifications, $\Delta\mu \gtrsim 0.4$, the more compact subhaloes are favored. Thus, the observed anomalies ($\Delta\mu \sim -0.25$) indicate that the subhaloes can not be very compact.

5   Conclusions

In this TFM we have studied the impact of the compactness of two different populations of millilenses (either BH's clusters or subhaloes) in the alteration of the intrinsic flux ratios between the images of lensed quasars. We have simulated the millilensing effect using inverse ray tracing algorithms coded in both Python3 and FORTRAN95. The main results of this TFM are;

1. The implementation of the nearest neighbours algorithm in the IRS code resulted in more accurate magnification maps (and PDF's), although the tail of the PDF's is still affected by the finite size of the pixel.

2. We have achieved a considerable reduction (by a factor > 17) of execution time by changing the millilensing code from Python3 to FORTRAN95.

3. Our numerical simulations reproduce the theoretical results for $PDF(\mu)$ in the sparse case limit for both, the BH's and the Gaussians subhaloes.

4. We have explicitly shown the pseudo-particle limit for clusters: if a cluster is small enough the resulting $PDF(\mu)$ is indistinguishable from the $PDF(\mu)$ produced by a point lens with the same mass than the cluster.

5. Since we are working with clusters that behave like pseudo-particles of mass the sum of the masses of the individuals BH's, the number of pseudo-particles per magnification map will be relatively small and, consequently, the spatial cluster distribution will be significantly affected by random fluctuations. For this reason it is necessary to average the PDF's from many single realizations (50 individual maps) to reduce sample variance.

6. We have obtained $PDF(\mu)$ for clusters of different compactness varying the number of BH's per cluster obtaining that the probability of large magnifications increase with compactness.

7. A Bayesian analysis based in our simulated $PDF(\mu|Nbh)$ and in typical values of the flux anomalies in lensed quasars indicates that clustering makes more unlikely the observations respect to a random uniform distributions of BH's.

8. We have derived $PDF(\mu)$ for Gaussian subhaloes with different compactness concluding that the probability of large magnifications increases with compactness. A Bayesian analysis based in our simulated $PDF(\mu|\sigma)$ and typical flux ratio anomalies indicates that according to the observations subhaloes of high compactness are unlikely.

6   Appendix

6.1   Python3 and FORTRAN95 scripts

In this section we are writing the codes used in Python3 and Fortran95 in order to perform the simulations.

Therefore, the code to generate a data file of a random uniform distribution of BH's is:

```python
import numpy as np
from matplotlib import pyplot as plt
from datetime import datetime

startTime = datetime.now()

gamma=0.45
kappa=0.45
kappa_smooth=0.
min_mass=0.999
max_mass=1.001
ny=1000
yl=50

allowance1=2
allowance2=1.5
xl=allowance1*yl/(1-kappa-gamma)

XL=5.*xl
num_bh=round(kappa*(2*XL)**2/np.pi)

rl=allowance2*np.sqrt(2)*xl

num=1
for abc in range(50):

    M=np.random.uniform(min_mass,max_mass,num_bh)
    x01=np.random.uniform(-XL,XL,num_bh)
    x02=np.random.uniform(-XL,XL,num_bh)

    fig, ax = plt.subplots()
    plt.scatter(x01,x02,color='green',sizes=np.array([0.001]*len(x01)))

    mask = x01**2+x02**2<=rl**2
    x01=x01[mask]
    x02=x02[mask]
    plt.scatter(x01,x02,color='blue',sizes=np.array([0.001]*len(x01)))

    #Save Data File
    data=np.empty((len(x01),3))
    for i in range(len(x01)):
        data[i,0]=x01[i]
        data[i,1]=x02[i]
        data[i,2]=M[i]

    np.savetxt('stars_uniform_dist_'+str(num)+'.dat', data)
    plt.xlabel('ER');plt.ylabel('ER')
    ax.set_box_aspect(1)
    plt.savefig('stars_uniform_dist_'+str(num),dpi=300)
    num+=1
    plt.show()

print(datetime.now() - startTime)
```

and the code to generate data file of a clustered distribution of BH's is:

```python
radius=4
bh_por_cluster=40

import numpy as np
from matplotlib import pyplot as plt
from datetime import datetime
```

```python
startTime = datetime.now()

def clustering(x_centre,y_centre,R):
        r=R*np.random.rand()
        theta=2*np.pi*np.random.rand()
        x01=r*np.cos(theta)+x_centre
        x02=r*np.sin(theta)+y_centre
        #print((x01-x_centre)**2+(x02-y_centre)**2<=R**2)
        return x01,x02

gamma=0.45
kappa=0.45
kappa_smooth=0.
min_mass=0.999
max_mass=1.001
ny=1000
yl=50

allowance1=2
allowance2=1.5
xl=allowance1*yl/(1-kappa-gamma)

XL=5.*xl
num_bh=round(kappa*(2*XL)**2/np.pi)

rl=allowance2*np.sqrt(2)*xl

num=1
for abc in range(50):

    M=np.random.uniform(min_mass,max_mass,num_bh)

    #Clusters
    num_clusters=num_bh//bh_por_cluster

    x_centre=2*XL*np.random.rand(num_clusters)-XL
    y_centre=2*XL*np.random.rand(num_clusters)-XL

    radii=np.array([radius]*num_clusters)

    #BH's
    x01=np.empty((num_clusters,num_bh//num_clusters))
    x02=np.empty((num_clusters,num_bh//num_clusters))

    for j in range(num_clusters):
        for i in range(num_bh//num_clusters):
            x01[j,i],x02[j,i]=clustering(x_centre[j],y_centre[j],radii[j])

    x01=x01.flatten()
    x02=x02.flatten()

    #We add the missing BH's
    for j in range(num_bh-num_clusters*int(num_bh/num_clusters)):
        x,y=clustering(x_centre[j],y_centre[j],radii[j])
        x01=np.append(x01,x)
        x02=np.append(x02,y)

    mask = x01**2+x02**2<=rl**2
    x01=x01[mask]
    x02=x02[mask]

    #Save Data File
    data=np.empty((len(x01),3))
    for i in range(len(x01)):
        data[i,0]=x01[i]
        data[i,1]=x02[i]
        data[i,2]=M[i]

    np.savetxt('stars_'+str(num)+'.dat', data)
    num+=1
```

```
print(datetime.now() - startTime)
```

The millilensing algorithm is done in FORTRAN95:

```fortran
module StarModule
  implicit none
  integer, parameter :: num_bh = 2000
  real(8) :: x01(num_bh), x02(num_bh), mass(num_bh)

contains

  subroutine ReadStars(input_file)
    character(len=*), intent(in) :: input_file
    integer :: i, ios
    open(unit=10, file=input_file, status='old', action='read')

    do i = 1, num_bh
      read(10, *, iostat=ios) x01(i), x02(i), mass(i)
      if (ios /= 0) exit
    end do

    close(10)
  end subroutine ReadStars

end module StarModule


PROGRAM Magnification
  USE OMP_LIB
  use StarModule
  IMPLICIT NONE

  INTEGER :: ny, nx
  REAL(KIND=8) :: shear, kappa, kappa_smooth, yl, xl
  REAL(KIND=8) :: min_mass, max_mass
  REAL(KIND=8) :: xs, ys
  real(8), allocatable :: A(:,:)
  REAL(KIND=8) :: x1, x2, y1, y2, r1, r2
  REAL(KIND=8) :: Area_A, Area_B, Area_C, Area_D
  REAL(KIND=8) :: mean_th, mag_nolensing
  INTEGER :: unit_number,the_unit, estado,i, j1, j2, i1, i2
  REAL(KIND=8), ALLOCATABLE :: d(:)
  REAL(KIND=8) :: sigma
  real(8) :: T1,T2
  integer :: argc
  character(len=30) :: input_file, output_file
  call cpu_time(T1)

  ! Get input and output filenames from command-line arguments
  call get_command_argument(1, input_file)
  call get_command_argument(2, output_file)
  call ReadStars(input_file)
  !call PrintStars(output_file)
  ALLOCATE(d(num_bh))

  !!!!!!!!!!!!!!!!!!!!!!!!!!!!!!!!!!!!!!!!!!!!!!!!!!!!!!!!!!!!!!!!!!!!!!!!
  !sigma=0.01
  !!!!!!!!!!!!!!!!!!!!!!!!!!!!!!!!!!!!!!!!!!!!!!!!!!!!!!!!!!!!!!!!!!!!!!!!
  kappa=0.1
  kappa_smooth=0.0
  shear=0.0
  ny=1000
  nx=10000
  yl=60.
  xl=100.

  !!!!!!!!!!!!!!!!!!!!!!!!!!!!!!!!!!!!!!!!!!!!!!!!!!!!!!!!!!!!!!!!!!!!!!!!
  !!!!!!!!!!!!!!!!!!!!!!!!!!!!!!!!!!!!!!!!!!!!!!!!!!!!!!!!!!!!!!!!!!!!!!!!

  ALLOCATE(A(ny,ny))

  mag_nolensing=(yl**2*(real(nx)-1)**2)/(xl**2*(real(ny)-1)**2)
```

```fortran
  ! Cell/Pixel size
  xs=2.0*xl/REAL(nx-1)
  ys=2.0*yl/REAL(ny-1)
  mean_th=1.0/((1.0-shear-kappa)*(1.0+shear-kappa))

  ! Magnification Map
  A = 0.0

  ! Loop
  !$OMP PARALLEL DO PRIVATE(j1,j2,i,d,y1,y2,i1,i2,r1,r2) shared(nx,num_bh,xl,xs,
  kappa,shear,x01,x02,sigma,yl,y2,ny,A)
  DO j1 = 1, nx-1
    !$OMP PARALLEL DO PRIVATE(i,d,y1,y2,i1,i2,r1,r2) shared(j1,j2,num_bh,x1,x2,
    x01,x02,sigma,yl,ys,ny,A)
    DO j2 = 1, nx-1
      ! Pixels to Coordinates
      x1=-xl+REAL(j1-1)*xs
      x2=-xl+REAL(j2-1)*xs

      ! Lense
      y1=x1*(1.0-kappa_smooth-shear)
      y2=x2*(1.0-kappa_smooth+shear)
      DO i = 1, num_bh
        d(i)=(x1-x01(i))**2+(x2-x02(i))**2+1.0E-12
        y1=y1-mass(i)*((x1-x01(i))/d(i))!*ERF(abs((x1-x01(i))/(SQRT(2.0)*(sigma/1.0))))
        y2=y2-mass(i)*((x2-x02(i))/d(i))!*ERF(abs((x1-x01(i))/(SQRT(2.0)*(sigma/1.0))))
      END DO

      ! Coordinates to Pixels
      i1=int((y1+yl)/ys+1)
      i2=int((y2+yl)/ys+1)

      ! Nearest Neighbours Algorithm
      r1 = ((y1+yl)/ys+1)
      r2 = ((y2+yl)/ys+1)

      Area_A=ABS((r1+1-INT(r1+1))*(r2+1-INT(r2+1)))
      Area_B=ABS((r1-INT(r1+1))*(r2+1-INT(r2+1)))
      Area_C=ABS((r1-INT(r1+1))*(r2-INT(r2+1)))
      Area_D=ABS((r1+1-INT(r1+1))*(r2-INT(r2+1)))

      IF ((i1.ge.1).and.(i1.le.ny).and.(i2.ge.1).and.(i2.le.ny)) THEN
        A(i1,i2)=A(i1,i2)+Area_C
        IF (i1+1.le.ny) THEN
          A(i1+1,i2)=A(i1+1,i2)+Area_D
        END IF
        IF (i2+1.le.ny) THEN
          A(i1,i2+1)=A(i1,i2+1) + Area_B
        END IF
        IF (i1+1.le.ny .AND. i2+1.le.ny) THEN
          A(i1+1,i2+1)=A(i1+1,i2+1)+Area_A
        END IF
      END IF
    END DO
  END DO
  !$OMP END PARALLEL DO
  END DO
  !$OMP END PARALLEL DO

  call cpu_time(T2)
  ! Open the output file and write the magnification map
  open(unit=20, file=output_file, status='replace', action='write')
  write(20, *) A/mag_nolensing
  close(20)
  WRITE(*, *) TRIM(output_file)

END PROGRAM Magnification
```

Additionally, we have developed an algorithm to plot the magnification maps and the histograms:

```python
import numpy as np
from matplotlib import pyplot as plt
```

```python
from datetime import datetime
startTime = datetime.now()

#############################################
sigma=1.
#############################################
kappa=0.1
kappa_smooth=0.
gamma=0.
min_mass=0.999
max_mass=1.001
ny=1000
nx=50000
yl=60.
xl=1.5*max(yl/(1-kappa-gamma),yl/(1-kappa+gamma))
num_bh=round(kappa*(2*xl)**2/np.pi)

mean_th=1.0/((1.0-gamma-kappa)*(1.0+gamma-kappa))
Magnification=np.loadtxt('Magnification_1.out', dtype=float)
A=Magnification.reshape((ny,ny))

#Magnification Map
plt.matshow(A)
plt.title('Magnification Map'+' yl = '+str(yl)+' \u03C3 = '+str(sigma))
plt.savefig('Magnification_map_sigma1',dpi=300)
plt.show()

#Magnification Histogram
A+=10**-12
mean=np.mean(A)

bins=np.linspace(-2.7,2.7,1000)
Delta_mu=-2.5*np.log10(A.flatten()/mean_th)
hist=np.histogram(Delta_mu,bins)
bincenters=0.5*(hist[1][1:]+hist[1][:-1])

integral=sum(hist[0])
DeltaMu=bincenters[1]-bincenters[0]
Const=1/(integral*DeltaMu)

plt.figure()
plt.plot(bincenters,Const*hist[0])
plt.xlabel('\u0394\u03BC(mag)')
plt.ylabel('log10(PDF)');plt.yscale('log')
plt.ylim(10**-4,1000)
plt.title('Magnification Histogram'+' yl = '+str(yl)+' \u03C3 = '+str(sigma))
plt.savefig('Magnification_Histogram_sigma1',dpi=300);plt.show()
print(datetime.now() - startTime)
```

6.2 Training

We started the TFM learning and checking the use of the algorithms, recreating real gravitational lens systems. Figures 29, 30 and 31 show real strong lensing events and the recreation performed by the algorithm.

(a) Real gravitational lens event; B1422+231.

(b) Resultant image of the source magnified recreating the event B1422+231.

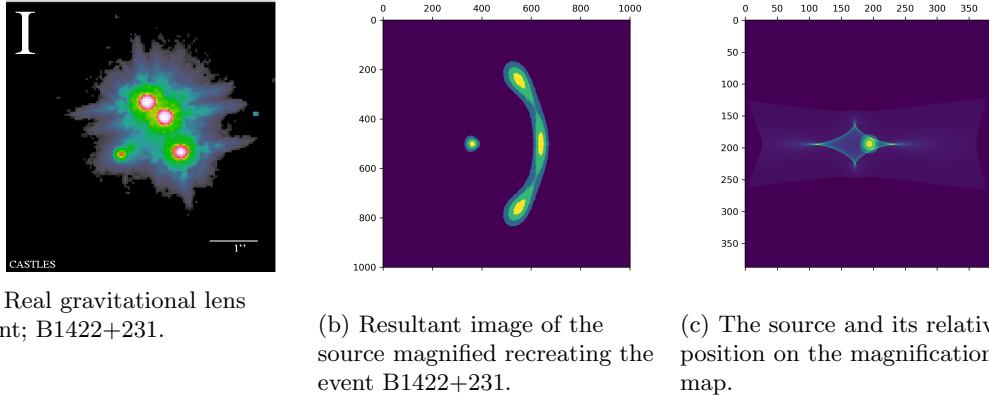(c) The source and its relative position on the magnification map.

Figure 29: Recreation of the gravitational lens event B1422+231. It is used a SIS with quadrupolar perturbation, the relative position of the source at the magnification map is at one of the vertex of the diamond.
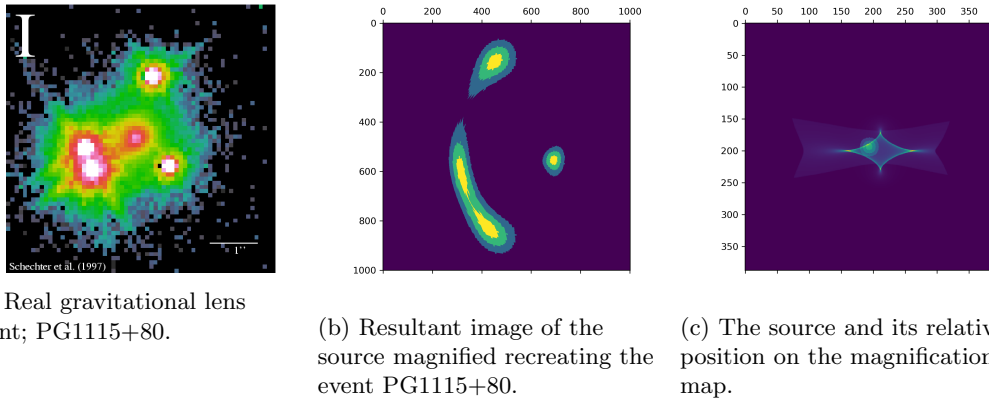

(a) Real gravitational lens event; PG1115+80.

(b) Resultant image of the source magnified recreating the event PG1115+80.

(c) The source and its relative position on the magnification map.

Figure 30: Recreation of the gravitational lens event PG1115+80. It is used a SIS with quadrupolar perturbation, the relative position of the source at the magnification map is at one of the sides of the diamond.

(a) Real gravitational lens event; B1938+666.

(b) Resultant image of the source magnified recreating the event B1938+666.

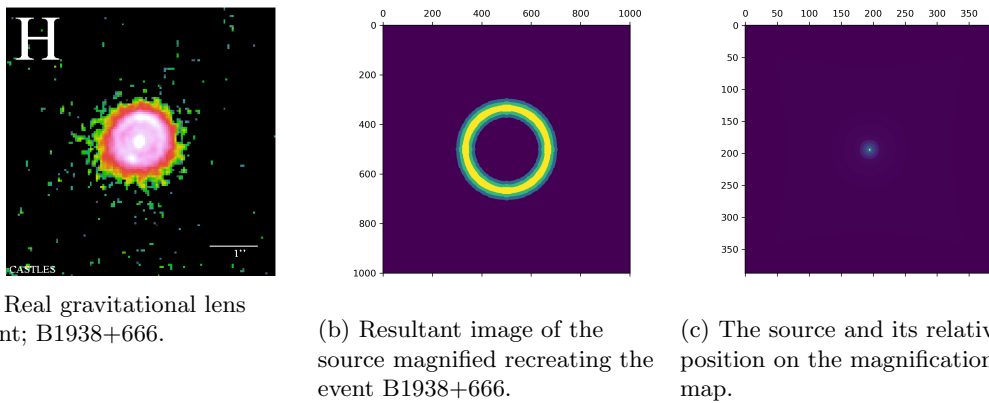(c) The source and its relative position on the magnification map.

Figure 31: Recreation of the gravitational lens event B1938+666. In this case it is used a isotherm sphere (Eq. 16), to produce an Einstein Ring, the source and the lens must be aligned.

As we can see, the script is able to recreate different strong lensing events. For all of them we have used a SIS+Qp lens (Eq. 17), but for the case of Figure 31 where we have used a SIS (Eq. 16).

Furthermore, the animation shows on the left side the magnification map with the caustics produced by the lens, and the relative position of the source respect to the lens. On the right side the animation shows the image of the source produced by the lens. In this case we have used also a SIS with a quadrupolar perturbation (Eq. 17).

.
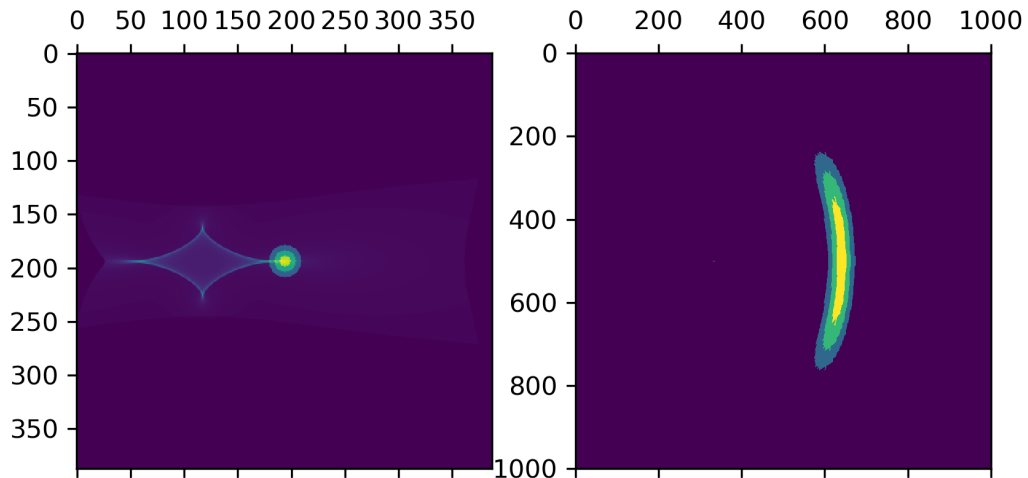
6.3 Extra Magnification Maps and BH's distribution for Clustering cases, with size $R_{cluster} = 4ER$

In this appendix we are going to add some magnification maps examples that were used on the TFM, for the clustering cases.

In Figure 32 we show the BH's distribution and magnification map of one case with $R_{cluster} = 4ER$ and 10 bh per cluster.
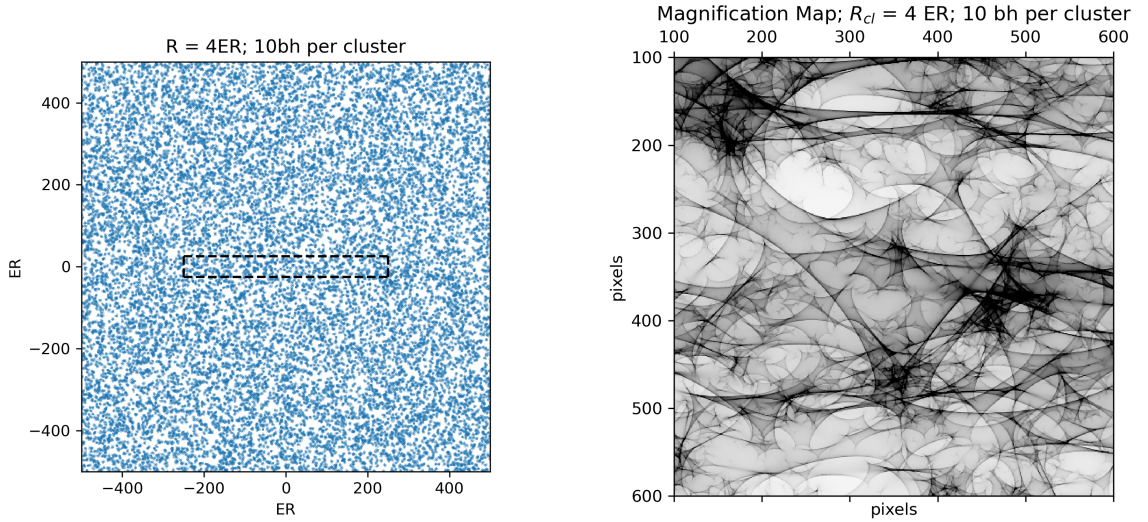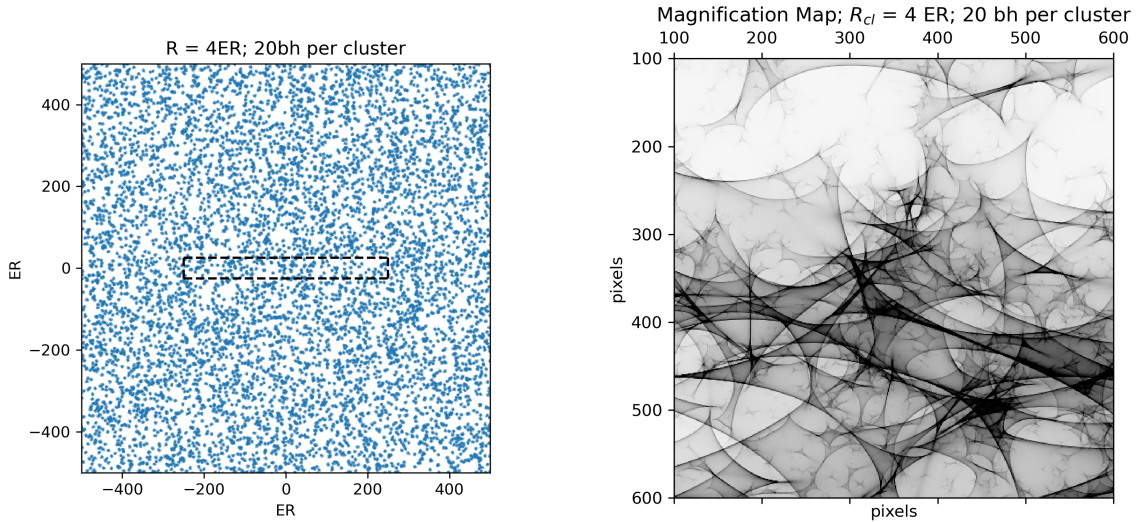
(a) Clustered distribution of BH's, with clusters of $R_{cluster} = 4ER$ and 10 BH per cluster.

(b) Magnification map of a clustered distribution of BH's, with clusters of $R_{cluster} = 4ER$ and 10 BH per cluster.

Figure 32: Clustered distribution of BH's and its magnification map, considering $y_l = 50ER$, $ny = 1000$, $\gamma = 0.45$, $\kappa_* = 0.45$, $\kappa_s = 0.0$, a minimum mass of 0.999 and a maximum mass of 1.001.

In Figure 33 we show the BH's distribution and magnification map of one case with $R_{cluster} = 4ER$ and 20 bh per cluster.
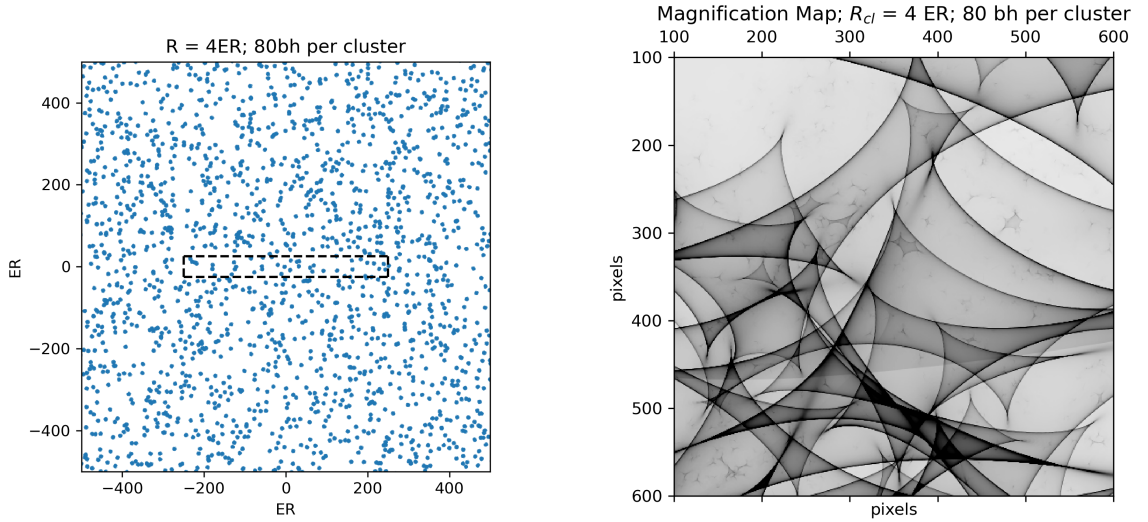

(a) Clustered distribution of BH's, with clusters of $R_{cluster} = 4ER$ and 20 BH per cluster.

(b) Magnification map of a clustered distribution of BH's, with clusters of $R_{cluster} = 4ER$ and 20 BH per cluster.

Figure 33: Clustered distribution of BH's and its magnification map, considering $y_l = 50ER$, $ny = 1000$, $\gamma = 0.45$, $\kappa_* = 0.45$, $\kappa_s = 0.0$, a minimum mass of 0.999 and a maximum mass of 1.001.

In Figure 34 we show the BH's distribution and magnification map of one case with $R_{cluster} = 4ER$ and 80 bh per cluster.

(a) Clustered distribution of BH's, with clusters of $R_{cluster} = 4ER$ and 80 BH per cluster.

(b) Magnification map of a clustered distribution of BH's, with clusters of $R_{cluster} = 4ER$ and 80 BH per cluster.

Figure 34: Clustered distribution of BH's and its magnification map, considering $y_l = 50ER$, $ny = 1000$, $\gamma = 0.45$, $\kappa_* = 0.45$, $\kappa_s = 0.0$ a minimum mass of 0.999 and a maximum mass of 1.001.

6.4 Extra case, with Constant size $R_{cluster} = 7ER$ and variable number of bh

We have done an extra clustering case considering also a constant size for the clusters $R_{cluster} = 7ER$, also considering $y_l = 50ER$, $ny = 1000$, $\gamma = 0.45$, $\kappa_* = 0.45$, $\kappa_s = 0.0$ a minimum mass of 0.999 and a maximum mass of 1.001. The theoretical magnification for these parameters is 10.0 mag (Eq. 20). Thus, we can see the effect of the clustering with different size by comparing it with the previous case with size $R_{cluster} = 4ER$.

In Figure 35 we can see the $PDF(\mu)$ histograms corresponding to the cases with the same size ($R_{cluster} = 7ER$) but varying the number of BH's per cluster, compared with the random uniform distribution case.
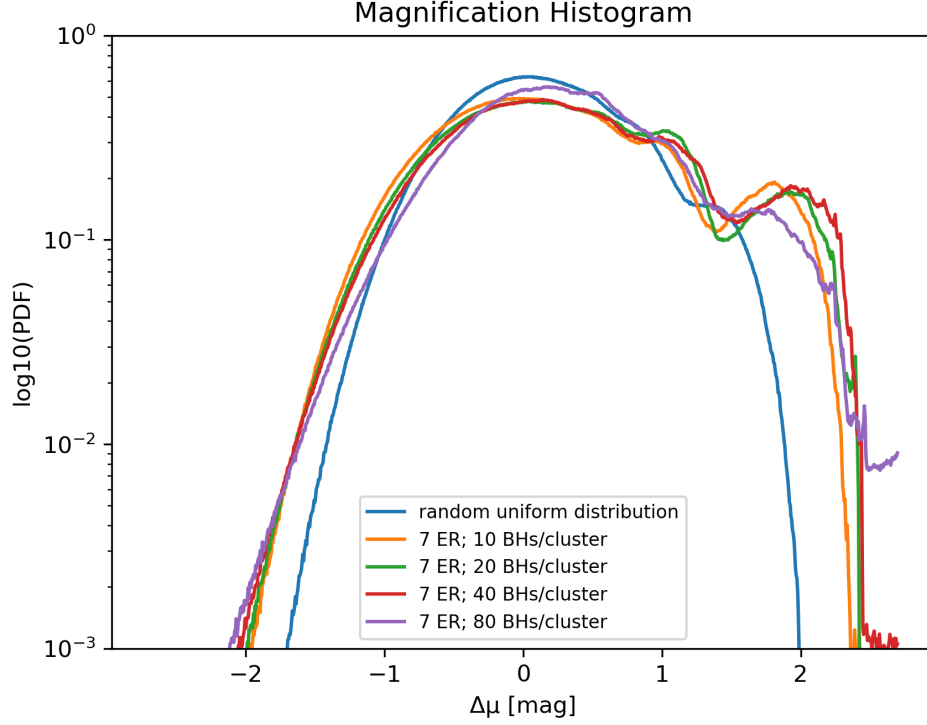
Figure 35: Averaged magnification histogram of 50 maps, each with a constant size of $R_{cluster} = 7ER$ and varying numbers of BH's per cluster: 10 bh (orange) with a mean magnification of 10.14 mag, 20 bh (green) with a mean magnification of 9.58 mag, 40 bh (red) with a mean magnification of 9.31 mag, 80 bh (purple) with a mean magnification of 9.01 mag, compared with the random uniform distribution (blue) with a mean magnification of 9.94 mag.

As in the previous case with $R_{cluster} = 4ER$, it can be seen in Figure 35 that the probabilities of large magnifications increase with compactness. Furthermore, with the decrease of the number of BH's per cluster, the shape of the histograms tends to be narrower being the random uniform distribution of BH's their limit.
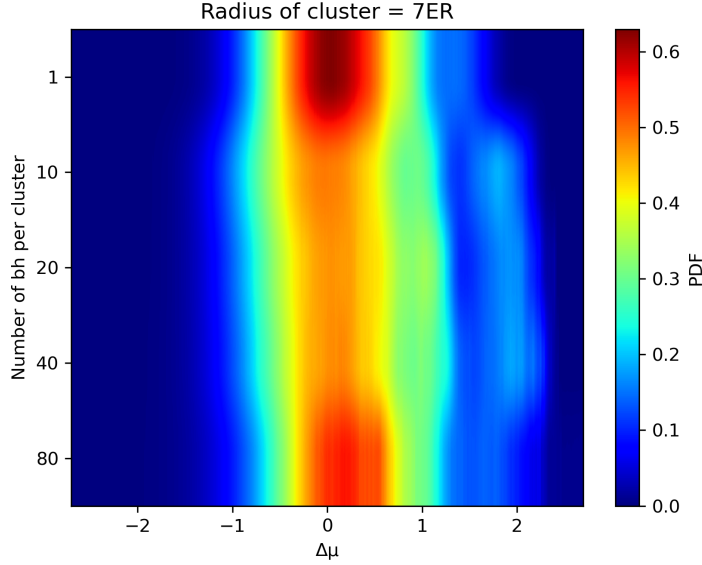
Figure 36: 2D PDF depending on the number of BH per cluster and the magnification, considering clusters with $R_{cluster} = 7ER$.

The Figure 36 shows the 2D PDF depending on the clumpiness and the magnification, for the case of clusters with constant size, $R_{cluster} = 7ER$. From the simulated data obtained in Figure 35.
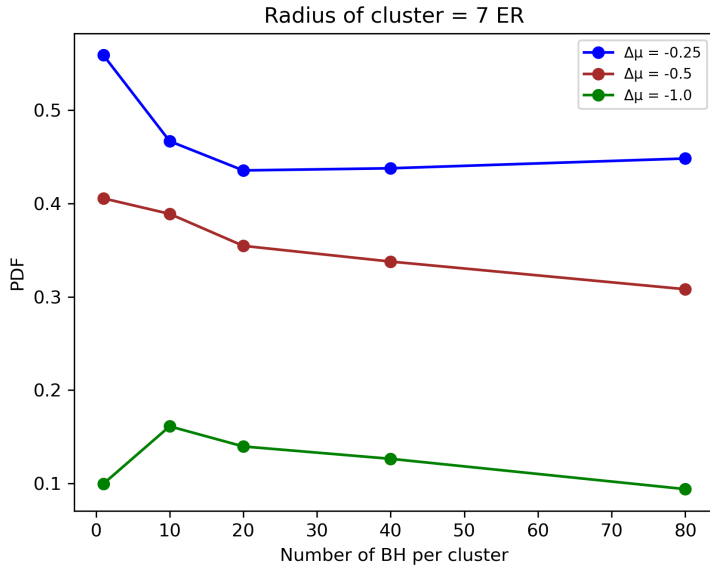

Figure 37: Probability density functions $PDF(\mu)$ vs number of BH's per cluster, for the different microlensing magnifications, considering clusters with $R_{cluster} = 7ER$.

Similarly to the previous case with $R_{cluster} = 4ER$, we can conclude from Figures 36 and 37 that the uniform distribution has more probability to generate typical magnifications than the clustered distributions.

We had to be careful selecting the sizes of the clusters, because if we select a cluster size that is too large they would intersect between them generating pseudo-clusters instead of dissolve, that is what we are looking for, so they tend to the random uniform distribution case.

References

[1] Evencio Mediavilla, J Jiménez-Vicente, and Muñoz. Chapter 24 lensing constraints: Substellar to intermediate masses.

[2] Konstantin M Belotsky, Vyacheslav I Dokuchaev, Yury N Eroshenko, Ekaterina A Esipova, Maxim Yu Khlopov, Leonid A Khromykh, Alexander A Kirillov, Valeriy V Nikulin, Sergey G Rubin, and Igor V Svadkovsky. Clusters of primordial black holes. *The European Physical Journal C*, 79:1–20, 2019.

[3] Jorge Jiménez-Vicente and E Mediavilla. Fast multipole method for gravitational lensing: Application to high-magnification quasar microlensing. *The Astrophysical Journal*, 941(1):80, 2022.

[4] Arthur B Congdon and Charles R Keeton. *Principles of gravitational lensing*, volume 10. Springer, 2018.

[5] Peter Coles. *Cosmology: A very short introduction*. OUP Oxford, 2001.

[6] Peter Schneider. *Extragalactic astronomy and cosmology: an introduction*, volume 146. Springer, 2006.

[7] Evencio Mediavilla, J Jiménez-Vicente, JA Muñoz, H Vives-Arias, and J Calderón-Infante. Limits on the mass and abundance of primordial black holes from quasar gravitational microlensing. *The Astrophysical Journal Letters*, 836(2):L18, 2017.

[8] Héctor Vives-Arias, Jorge Jiménez-Vicente, Jose A Muñoz, and Evencio Mediavilla. Estimating the size and abundance of dark matter subhaloes with gravitational millilensing. *MNRAS*, 454:287, 2015.

[9] A Esteban-Gutiérrez, N Agües-Paszkowsky, E Mediavilla, J Jiménez-Vicente, JA Muñoz, and S Heydenreich. The impact of the mass spectrum of lenses in quasar microlensing studies. constraints on a mixed population of primordial black holes and stars. *The Astrophysical Journal*, 904(2):176, 2020.

[10] Heydenreich, S. et al. 2024, submitted.